Published in final edited form as:

Prog Neurobiol. 2022 June ; 213: 102264. doi:10.1016/j.pneurobio.2022.102264.

Ultrastructural view of astrocyte arborization, astrocyte-astrocyte and astrocyte-synapse contacts, intracellular vesicle-like structures, and mitochondrial network

Sydney Aten[1,¶,†], **Conrad M. Kiyoshi**[1,¥,†], **Emily P. Arzola**[1,‡], **Jeremy A. Patterson**[2], **Anne T. Taylor**[1], **Yixing Du**[1], **Ally M. Guiher**[1], **Merna Philip**[1], **Elizabeth Gerviacio Camacho**[1], **Devin Mediratta**[1], **Kelsey Collins**[1], **Kirsten Boni**[1,4], **Silvana A. Garcia**[1,4], **Rahul Kumar**[1], **Aiden N. Drake**[1], **Ahlam Hegazi**[1], **Lindsey Trank**[1], **Emily Benson**[3], **Grahame Kidd**[3], **David Terman**[4], **Min Zhou**[1,*]

[1]Department of Neuroscience, Ohio State University, Columbus, OH, USA

[2]Advanced Computing Center for the Arts and Design, Ohio State University, Columbus, OH, USA

[*]**Corresponding Author:** Dr. Min Zhou, Department of Neuroscience, Ohio State University; Phone: 614-366-9406; Fax: 614-688-8742; zhou.787@osu.edu.

[¶]Present address: Department of Neurology, Division of Sleep Medicine, and Program in Neuroscience, Harvard Medical School, Beth Israel Deaconess Medical Center, Boston, MA, USA.

[¥]Present address: Northern Marianas College, Saipan, MP, USA.

[‡]Present address: Case Western Reserve University School of Medicine., Cleveland, OH, USA.

[†]These authors contributed equally to this study

Author Contributions:

· Sydney Aten (Conceptualization, Data curation, Formal analysis, Funding acquisition, Investigation, Methodology, Validation, Visualization, Writing-original draft, Writing-review and editing)

· Conrad M. Kiyoshi (Conceptualization, Data curation, Formal analysis, Investigation, Methodology, Validation, Visualization, Writing-original draft, Writing-review and editing)

· Emily P. Arzola (Data curation, Formal analysis, Investigation, Methodology, Validation, Visualization, Writing-review and editing)

· Jeremy A. Patterson (Investigation, Methodology, Resources, Software, Visualization, Writing-review and editing)

· Anne T. Taylor (Data curation, Formal analysis, Writing-review and editing)

· Yixing Du (Data curation, Validation, Writing-review and editing)

· Ally M. Guiher (Data curation, Writing-review and editing)

· Merna Philip (Data curation, Writing-review and editing)

· Elizabeth Gerviacio Camacho (Data curation, Writing-review and editing)

· Devin Mediratta (Data curation, Writing-review and editing)

· Kelsey Collins (Data curation, Writing-review and editing)

· Kirsten Boni (Data curation, Writing-review and editing)

· Silvana A. Garcia (Data curation, Writing-review and editing)

· Rahul Kumar (Data curation, Writing-review and editing)

· Rahul Kumar (Data curation, Writing-review and editing)

· Aiden N. Drake (Data curation, Writing-review and editing)

· Ahlam Hegazi (Data curation, Writing-review and editing)

· Lindsey Trank (Data curation, Writing-review and editing)

· Emily Benson (Data curation, Resources, Software, Validation, Writing-review and editing)

· Grahame Kidd (Data curation, Resources, Software, Supervision, Validation, Writing-review and editing)

· David Terman (Conceptualization, Formal analysis, Funding Acquisition, Investigation, Methodology, Resources, Software, Validation, Visualization, Writing-review and editing)

· Min Zhou (Conceptualization, Formal analysis, Funding acquisition, Investigation, Methodology, Project administration, Resources, Supervision, Validation, Visualization, Writing-original draft, Writing-review and editing).

Conflict of Interest Statement:

The authors declare no competing interests.

[3]Lerner Research Institute, Cleveland Clinic, Cleveland, OH, USA.

[4]Department of Mathematics, Ohio State University, Columbus, OH, USA

Abstract

The complexity of astrocyte morphology and syncytial coupling through gap junctions are crucial for astrocyte function in the brain. However, the ultrastructural details of astrocyte arborization and interactions between neighboring astrocytes remain unknown. While a prevailing view is that synapses selectively contact peripheral astrocyte processes, the precise spatial-location selectivity of synapses abutting astrocytes is unresolved. Additionally, knowing the location and quantity of vesicles and mitochondria are prerequisites to answer two emerging questions - whether astrocytes have a signaling role within the brain and whether astrocytes are highly metabolically active. Here, we provided structural context for these questions by tracing and 3D reconstructing three neighboring astrocytes using serial block-face scanning electron microscopy. Our reconstructions reveal a spongiform astrocytic morphology resulting from the abundance of reflexive and leaflet processes. At the interfaces, varying sizes of astrocyte-astrocyte contacts were identified. Inside an astrocyte domain, synapses contact the entire astrocyte, and synapse-astrocyte contacts increase from soma to leaflets. In contrast to densely packed vesicles at synaptic boutons, vesicle-like structures were scant within astrocytes. Lastly, astrocytes contain dense mitochondrial networks with a mitochondrial volume ratio similar to that of neurites. Together, these ultrastructural details should expand our understanding of functional astrocyte-astrocyte and astrocyte-neuron interactions.

Keywords

Astrocyte network; *Aldh1l1*-eGFP; serial blockface scanning electron microscopy (SBF-SEM); three-dimensional reconstruction; synaptic-like microvesicles; synapses; mitochondria

Introduction:

The complexity of the cellular morphology of astrocytes is essential for their function in the brain. Among diverse subtypes of astrocytes, protoplasmic astrocytes establish spatially distinct domains with minimal overlap at their interface boundaries (Bushong *et al.*, 2002; Halassa *et al.*, 2007; Ogata and Kosaka, 2002; Xu *et al.*, 2014). However, with respect to astrocytic branching patterns, two models are still highly debated. One model postulates that astrocytes follow a tree-like dendritic architecture (reminiscent of most neural cells), while others favor a mesh-like spongiform architecture established through internal connectivity via branch fusions or reflexive gap junctions (Khakh and Sofroniew, 2015a; Rusakov, 2015).

Gap junction mediated syncytial coupling adds another layer of complexity to the spatial architecture of astrocytes (Gutnick *et al.*, 1981; Muller, 1996; Nagy and Rash, 2003). Indeed, syncytial coupling allows astrocytes to function beyond the single-cell level, enabling them to work as a cohesive unit in brain homeostasis and signaling (Giaume *et al.*, 2010; Kiyoshi and Zhou, 2019; Rose and Chatton, 2016; Stephan *et al.*, 2021). However, aside from a well-established knowledge that astrocytes only make contact at their domain interfaces

with less than 10% of processes (Bushong *et al.*, 2002), an ultrastructural view of these inter-astrocyte contacts has yet to be resolved.

Inside the domains, each astrocyte makes contact with thousands of synapses (Bushong *et al.*, 2002), and thus, astrocytes contribute (as the 'third party') to influence synaptic transmission and plasticity (Araque *et al.*, 1999; Perea *et al.*, 2009). An unanswered question, however, is the spatial-location selectivity of synapses within this astrocyte domain. Along these lines, it remains unknown whether synapses selectively make contact with the terminal processes, termed 'leaflets' (Gavrilov *et al.*, 2018; Khakh and Sofroniew, 2015b; Peters and Palay, 1996), or whether they make contacts with the entire astrocyte (from soma to leaflets). Answering these unresolved questions would provide critical anatomic insights into the functional crosstalk between astrocytes and neurons.

Intracellular organelles are crucial structural elements for astrocyte function. For example, Ca^{2+}-dependent vesicular release of gliotransmitters has been shown to mediate astrocyte-neuron crosstalk (Pascual *et al.*, 2005; Perea and Araque, 2007). While the location and quantity of synaptic-like microvesicles (SLMVs) is crucial to the understanding of how astrocytes influence synaptic transmission, the small-volume representation of astrocytes in the neuropil (5–7%), relative to neurons (70–75%), makes tracing and quantification of SLMVs from small-sample EM data much less reliable (Medvedev *et al.*, 2014; Rusakov, 2015). An additional organelle that is crucial to the overall functionality of the cell is mitochondria. Currently, astrocytes are viewed as energy-saving cells given that they are electrically non-excitable (Attwell and Laughlin, 2001). However, increasing evidence indicates an abundance of mitochondria in astrocytic processes (Agarwal *et al.*, 2017; Chai *et al.*, 2017; Lovatt *et al.*, 2007). Interestingly, astrocytes also express higher levels of enzymes in the tricarboxylic acid cycle compared to neurons (Lovatt *et al.*, 2007), and this is correlated with a comparably higher oxidative capacity of astrocytes (relative to neurons) in functional PET studies (Wyss *et al.*, 2009). Thus, knowing the distribution and quantity of mitochondria should yield significant insights into the energy metabolism of astrocytes.

Answers to these aforementioned questions rely on the ability to resolve the ultrastructural entirety of astrocytes and the contacts between astrocytes and other constituents in the brain. In the present study, we used serial blockface scanning electron microscope (SBF-SEM) to minimize the preparation damage to the fine nanoscopic astrocytic processes (Denk and Horstmann, 2004; Ventura and Harris, 1999) and to identify and reconstruct three neighboring astrocytes. Notably, we prepared our EM specimen from an adult P45 *Aldh1l1*-eGFP transgenic mouse, wherein astrocytes were identity-validated and location-defined. This allowed us to utilize a novel, "inside-out' EM sketching approach (i.e., tracing three neighboring astrocytes from the soma to the leaflet processes).

Here, we reconstructed - for the first time in requisite detail - the ultrastructure of an astrocyte connectome in an adult mouse hippocampus. Tracing and 3D reconstructing each of the three astrocytes allowed us to determine the branching pattern of astrocytic processes and to identify inter-astrocytic contacts. Further, by tracing and reconstructing three dendrites (and their contacting axons) located within our astrocyte connectome, we examined the spatial-location selectivity of astrocyte-synapse contacts. Analysis of these

astrocyte-synapse contacts revealed that synapses contact every physical compartment of an astrocyte and that there is a graded increase in synapse density from soma to leaflets. Finally, by tracing *all* mitochondria located within the three astrocytes and the three neurites, we found that astrocytes contain a comparable quantity of mitochondria relative to neurons.

Materials and Methods:

Experimental Model and Subject Details:

An adult, postnatal day 45, female BAC *Aldh1l1*-eGFP mouse was used in this study. Details of this mouse line have previously been reported (Kiyoshi *et al.*, 2018; Yang *et al.*, 2011). Mice were housed in a temperature-controlled (22 ± 2°C) environment with a 12 hour light/dark schedule and were given ad libitum access to food and water. All procedures were performed in accordance with a protocol approved by the Institutional Animal Care and Use Committee (IACUC) at The Ohio State University.

Tissue processing:

A postnatal day (P) 45 mouse was anesthetized with an intraperitoneal injection of 8% chloral hydrate in 0.9% saline and then transcardially perfused at 6 ml/min with 4% paraformaldehyde and % glutaraldehyde in 0.1 M sodium cacodylate buffer. Sodium cacodylate, paraformaldehyde, and shell vials were purchased from Electron Microscopy Sciences (Hatfield, PA, USA). 25% EM grade glutaraldehyde was purchased from Polysciences Inc (Warminster, PA, USA). Coronal CA1 hippocampal brain slices (300 μm) were then cut with a Vibratome (Pelco 1500) and post-fixed with the same fixative overnight (at 4 °C) in shell vials.

Correlative confocal and serial blockface scanning electron microscopy (SBF-SEM):

Each *Aldh1l1*-eGFP hippocampal brain slice was then imaged using a Leica (SP8) confocal microscope to obtain astrocyte spatial localization and blood vessel landmark visualization within the stratum radiatum. These confocal images were used to correlate and select a region of interest (ROI) for subsequent electron microscopy tissue processing.

After confocal images were acquired, fixed tissue sections were washed five times in 0.1 M sodium cacodylate, followed by staining with reduced osmium (2% osmium tetroxide and potassium ferrocyanide in 0.1 M sodium cacodylate buffer) at 4 °C for 2.5 hours (hr). Sections were then washed five times in double distilled water, followed by incubation in 1% thiocarbohydrazide at 60 °C for 1 hr, before being washed again in double-distilled water. Sections were then stained with 2% aqueous osmium tetroxide for 2 hr at room temperature and were subsequently incubated (for 24–30 hr) in aqueous uranyl acetate at 4 °C. Next, the tissue was washed and incubated for 60 minutes at 60 °C in Walton's lead aspartate, followed by washing in double distilled water before beginning dehydration through a series of incubations in ethyl alcohol, propylene oxide (4 hr), and 90 min in Epon 812-substitute resin before being embedded in Epon 812-substitute resin and left to cure for 48 hr at 60 °C. Next, the tissues were trimmed out of the resin and oriented on the pin according to the corner notch that was cut into the wet tissue before confocal imaging.

Here, we should note this EM specimen preparation is known to cause brain tissue to 'shrink' the extracellular space from the normal 20% to 1–2% (Hillman and Deutsch, 1978; Kalimo, 1976; Korogod *et al.*, 2015; Tonnesen *et al.*, 2018), and we did not incorporate a correction factor in our analyses. Thus, one should keep in mind that our sample volume is likely less than it was pre-EM processing.

The tissue was mounted on aluminum and coated with colloidal silver liquid around the exposed edges of the resin block. A Zeiss Sigma VP system (with an in-chamber Gatan 3 View ultamicrotome with low-kV backscattered electron detectors) was used to examine the tissue. Tissue samples were imaged at 2.2 kV, with 7.7 nm/pixel resolution. Slices were 75 μm thick. SBF-SEM image acquisition and registration were conducted at Renovo Neural (Cleveland, OH, USA). The total image scan size for the data set is 54.02 × 96.47 × 37.5 μm (X, Y, Z). Image series were registered and then analyzed using Reconstruct (see below).

Three-dimensional reconstructions of hippocampal astrocytes, neurites, blood vessels, and intracellular particles:

500 serial SBF-SEM images of the stratum radiatum (provided by Renovo Neural) were imported with image pixel size (0.0077 μm/pixel) and slice thickness (0.075 μm) into Reconstruct (Fiala, 2005). Cellular structures were traced manually or traced using the Reconstruct wildfire tool to generate individual objects. Structures traced with the wildfire tool were verified by several experimenters, and errors (if any) were manually corrected. The volume of each completed object was automatically generated in Reconstruct. The Z-trace tool was used to measure the dimensions (size, length, etc.) of each object, and the ellipse tool was used to trace rounded objects (such as glycogen granules). The line analysis tool from ImageJ was used to detect cellular contact(s) between two adjacent membranes where the membrane and extracellular space can be discerned by the black and white intensities, respectively (Schindelin *et al.*, 2012). To be considered a 'contact', no visible extracellular space between the two astrocyte processes could be observed. Completed Boissonnat surface object reconstructions were generated in Reconstruct and were then exported as VRML 2.0 files for further rendering in Blender (see below).

Visualizing SBF-SEM reconstructed data using Blender 2.78:

Blender - a free, open-source 3D, general-purpose graphics tool that allows for modeling of large-volume data sets - was used to reconstruct our astrocyte connectome files. Note that Blender has been used in several other studies examining EM neural tissues (Cali *et al.*, 2019; Cali *et al.*, 2016; Zheng *et al.*, 2018). VRML 2.0 files (created in Reconstruct) were imported into Blender and were then colored and rendered to obtain final 3D reconstructions. Note that in certain circumstances, objects were made slightly transparent (using the 'Z transparency' tool) to allow for easy visualization of multiple objects in contact with one another.

Blender video reconstructions and animations:

Blender (v2.90.0) - an open-source software package - was utilized to model, render, and animate the rasterized 3-dimensional astrocyte-neurite network visualizations. The visualizations convey complex structures, and therefore specific rendering and staging

techniques were used in the production process to ensure structures were visually distinct and to afford clarity to the represented forms. Along these lines, a two-source light design scheme was used for the videos, with one key light source positioned near the camera and a second source located in the subject's rear. The key light source illuminates the subject's front while reducing shadows that could obscure complex structures. The rear light source (referred to as a 'hair light') borrows from film lighting techniques to accentuate and define very fine structures.

Further, care was taken to ensure that shadows did not obscure the complex structures in the reconstructed video animations. Toward this end, the lighting that was utilized simulates area lights which allow for volumetric shadows that mimic naturally occurring soft shadows and approximate the light source's environmental diffusion, while also providing visual depth cues.

The rendered subject surfaces in the videos were achieved with two physically based rendering techniques - transmission and subsurface light scattering approximations - to obtain a volumetric design. These tactics act to soften the subject's surface features and convey a waxy, organic appearance. Additionally, this strategy allowed for light transmission through the objects' edges to create visual definition.

Calculation of the percentage of astrocytes reconstructed within EM block:

To estimate the percentage of the three astrocytes that were reconstructed within our EM volume, we followed a rationale described by Cali et al. (Cali *et al.*, 2019). Specifically, each protoplasmic astrocyte was assumed to be ellipsoid in shape. Along these lines, we first obtained multiple coordinates of points from the outer surface of the astrocytes in our EM stacks. We then fitted an ellipsoid to these points that lie on the outer surface of the cell (see Fig. S1) using the algorithm described in the following link: http://www.juddzone.com/ALGORITHMS/least_squares_3D_ellipsoid.html. Next, we calculated the percentage of the volume of the ellipsoid that was found within the bounding box, i.e., the rectangular shaped EM stack with a calculated volume of 1.95×10^5 μm^3.

Mathematical modeling of astrocyte contacts:

The Z-trace tool (Reconstruct) was used to measure the dimensions of astrocytic processes to be used in mathematical modeling simulations. To computationally model the effect of a cluster of astrocyte contacts on the coupling coefficient (CC), the area between the contacting astrocytes was measured using Reconstruct (these regions were the presumed sites of gap junctions). Further, the number of likely gap junctions was estimated based on the density of gap junctions from freeze-fracture replica immunogold labeling experiments (Rash *et al.*, 2001a; Rash *et al.*, 2001b). Note that morphometric data used for resistance calculations were derived from tracing the blue and pink astrocytes (see Fig. 1 for full reconstructions) from their somas to interface contacts. Astrocytic processes from the contact site (between the blue and pink astrocytes) were then segmented and numbered (Fig. S6 and Table S2), and key dimensions of these processes were measured to calculate the resistance (Table S3).

Each compartment in our multi-compartment representation of an astrocyte is modeled as a passive cable (Ermentrout and Terman, 2010) where the specific membrane and intracellular resistivity of each compartment are assumed to be 10^3 Ω cm^2 and 10^2 Ω cm, respectively. The specific membrane capacitance is 1 μF/cm^2. The cross-sectional areas and lengths of the compartments are given in Table S2.

Current across a gap junction is modeled as $(V_2\text{-}V_1)/R_{gap}$ where V_1 and V_2 are the membrane potentials at the compartments adjacent to the gap junction, and the current flows from blue astrocyte to pink astrocyte (Fig. S6). The gap junctional resistances, R_{gap}, were computed as follows: We first determined the areas of processes at the contacts, corresponding to the gap junctional interface. We then assumed that the density of gap junctions within this area is 10^3/μm^2 (Ma *et al.*, 2016). Moreover, each gap junction has a single-channel conductance of 60 pS and an open probability of 20% (Ma *et al.*, 2016). Therefore, if the interface area is A μm^2, then the number of gap junctions within the interface is $A/10^3$ and the total conductance is $12A/10^3$ pS. Hence, the total resistance is $10^9/12$ A MΩ. Values for the interface areas and gap junctional resistances are given in Table S3.

Analysis of synapse contact with various astrocyte process types:

Similar to the vesicle and glycogen granule analysis (described below), a 5 × 5 μm, 10 z-stack ROI was drawn around an astrocyte region (from a 2D EM trace). These regions included the astrocyte soma, root/branch, intermediate/branchlet, terminal/leaflet, reflexive, and endfeet processes. Three of these ROIs were drawn for each astrocyte region. The synapses that contacted a region of the astrocyte within that ROI were traced and the total number of synapses that contacted the astrocyte within the 10 z-stack ROI was divided by the total volume that the astrocyte occupied. This process was repeated for all regions of three different astrocytes.

Ultrastructural synapse-astrocyte contact analysis:

Analysis of astrocyte coverage of synapses was adapted from a recently published report (Kikuchi *et al.*, 2020). Note, however, that our analysis was conducted in SBF-SEM traces (i.e., 2-dimensional) and not in rendered (i.e., 3-dimensional) constructions. To begin, three complete dendrites (and their associated spines) were traced using Reconstruct. Axons that contacted each spine were also traced (in a retrograde manner) to completion. Here, it is important to mention that we only traced/reconstructed three complete neurites (for ease of viewing and for analytical purposes - as observed in Fig. 5); however, many more (untraced) neurites can be found within the EM reconstructed volume. Next, each synapse was marked and classified as asymmetric or symmetric based on whether the postsynaptic density was prominent (Gray, 1959; Kikuchi *et al.*, 2020; Peters and Palay, 1996) (see Fig. 7D1 for examples of the two types of synapses). Of note, the classification of synaptic junctions into asymmetric versus symmetric was based on a series of z-stack images in which the PSD was prominent/pronounced (Santuy *et al.*, 2020). Finally, the area surrounding each synapse was examined to determine whether any astrocyte processes were located adjacent to the synapse. Three categories were then established like classifications conducted by Kikuchi et al (Kikuchi *et al.*, 2020):

1. ‘Cleft associated astrocytes’ were those synapses whose synaptic clefts made contact with an astrocyte process.
2. ‘Pre/post associated astrocytes’ were those synapses whose pre- or post-synaptic elements made contact with an astrocyte process, but not with the cleft.
3. ‘Free astrocytes’ were those synapses that had no adjacent contacts with astrocyte processes.

Of note, if an astrocyte contacted both the synaptic cleft and a pre-or post-synaptic element, the contact was classified as ‘cleft contact’. The percentage of astrocyte (and non-astrocyte) associated synapses was then calculated from three dendrites.

Analysis of vesicle-like structures within astrocyte processes:

A 5 × 5 μm, 10 z-stack region-of-interest (ROI) was drawn around an astrocyte region (from a 2D EM trace). These regions included the astrocyte soma, root/branch, intermediate/branchlet, terminal/leaflet, reflexive, and endfeet processes. Three of these ROIs were drawn for each astrocyte region. The vesicle-like structures within each ROI were counted, and the total number of vesicle-like structures within each ROI was divided by the total volume that the astrocyte process occupied to determine the density of vesicle-like structures per volume of astrocyte (vesicle-like structures/μm^3). This process was replicated for all process types of three different astrocytes (blue, pink, and purple). Criterion used to identify vesicle-like structures can be found in Fig. S2. As a control, the total number of synaptic vesicles was also analyzed using these same parameters - 5 × 5 μm boxes from synapses surrounding the astrocyte soma were marked as ROIs. The number of vesicles (in the stacks where the synapse was prominent) was divided by the volume of the presynaptic element (which contained the vesicles) to determine the density of vesicles (vesicles/μm^3).

Analysis of glycogen granule content within astrocyte processes:

Glycogen granule density within various regions of astrocyte processes was also analyzed. For this analysis, a 5 × 5 μm, 10 z-stack ROI was drawn around an astrocyte region (from a 2D EM trace). These regions included the astrocyte soma, root/branch, intermediate/branchlet, terminal/leaflet, reflexive, and endfeet processes. Three of these ROIs were drawn for each astrocyte region, and data obtained from three total astrocytes was used for analysis (see Table S1). The glycogen granules within each specific astrocyte region (within the ROI) were traced using the Reconstruct ellipse tool, and the total number of glycogen granules within the 10 z-stack ROI was divided by the total volume that the astrocyte occupied. Criterion used to identify vesicle-like structures can be found in Fig. S2.

Analysis of mitochondria within astrocytes and neurites:

All mitochondria within the three reconstructed astrocytes and the three reconstructed neurites (dendrites and axons included) were traced and 3D-reconstructed. For analysis of leaflet process diameter versus mitochondria diameter (Fig. 10H), the diameter of 25 leaflet processes and 25 mitochondria was measured from each of the three astrocytes using the Reconstruct Z-trace tool.

To obtain the mitochondria to cell (i.e., astrocyte, dendrite, or axon) volume ratio (Fig. 11E), the volume of all mitochondria within each cell was compared to the overall volume of the cell (i.e., the volume of all mitochondria within the blue astrocyte was compared to the overall volume of the blue astrocyte). The ratio of the mitochondria to cell volume for the three astrocytes, the three dendrites, and the axons was then plotted graphically. Of note, because the somas for the three traced/reconstructed neurites were not found within our EM sample (i.e., the somas of the neurites were located outside of the sample volume used for EM imaging/reconstruction), the astrocyte somas (which were located within our EM sample volume) were not included in our analysis for the mitochondria to astrocyte volume ratio - to parallel our analysis of neurites.

Statistical Analysis:

All statistics were performed using GraphPad Prism 7.0 software, and group data are presented as mean ± SEM. Details of statistical tests (such as the test statistic, degrees of freedom, and p-value) can be found in the Results section (or supplementary tables) of the manuscript. As noted in the figure legends, significance was ascribed to p-values < 0.05. Further, comparisons between three (or more) groups/variables were conducted using a one-way ANOVA, followed by post-hoc analysis. For each experiment, Grubb's test was conducted on data obtained from each group to determine whether the outlier was statistically significant ($p < 0.05$). Hence, this test was used to exclude one data point (terminal/leaflet process ROI) from the analysis of vesicle-like structures within astrocytes (Fig. 9G). Additionally, Grubb's test was used to exclude three data points (one soma ROI and one reflexive ROI) from the analysis of synapse density in relation to astrocyte process type (Fig. 6H) and one soma ROI from the analysis of glycogen granule density (Table S1).

Results:

Identification, tracing, and 3D reconstruction of neighboring astrocytes

To prepare the specimen for SBF-SEM study, we used confocal microscopy to define the region of interest (ROI) that contained three neighboring astrocytes from an *Aldh1l1*-eGFP reporter mouse. Specifically, after tissue fixation, low magnification images of coronal brain sections encompassing the cortex and hippocampus were taken. An angular cut made in the cortex serves as a point of reference for orientation purposes (Fig. 1A1). Note that we selected a tissue section that contained visible blood vessels which could be used as landmarks. An area containing eGFP+ astrocytes next to a visibly large blood vessel in the stratum radiatum of the hippocampus was chosen as our ROI (Fig. 1A2). The tissue section containing the ROI was then processed for SBF-SEM (Fig. 1B).

According to the initial confocal locations, we first identified the somas of three *Aldh1l1*-eGFP astrocytes within the SBF-SEM dataset that contained the nucleus and their extended irregular and angular primary processes (see Fig. 1C). To further confirm their astrocytic identity, we then examined the key structural characteristics of astrocytes, which included glycogen granules and bundles of intermediate filaments (Fig. 1C and 1D; see Fig. S2 for glycogen granule identification criteria, Table S1 for relative glycogen granule density, and File S2 for glycogen granule density analysis). In addition, some of the terminal

processes formed characteristic endfeet that contacted blood vessels (Fig. 1E). Notably, these processes never made any distinct synaptic-like structures, therefore eliminating the possibility that they were neurons or NG2 glia (Bergles *et al.*, 2000).

Within the SBF-SEM dataset, we traced these astrocytes, (color-coded with purple, blue, and pink), and a surrounding blood vessel to completion. 3D reconstructions were then created (Fig. 1F–1H). As described in the Methods section, we calculated the approximate completion percentage of each of the three astrocytes, finding that the pink, blue, and purple astrocytes were 78.5%, 34.3%, and 96.9% complete, respectively (also see Fig. S1, Table S1, and File S1 for details). The volumes for each of the three astrocytes were estimated at 1.13×10^5 μm^3 (pink astrocyte), 5.7×10^4 μm^3 (blue astrocyte), and 4.14×10^4 μm^3 (purple astrocyte). Of note, the blue astrocyte was the least complete because this cell was only partially included in the EM specimen (i.e., the bottom half of the blue astrocyte was cut-off in the data set (Fig. 1G)); hence, it is also smaller in appearance. Merging the three astrocytes created a 3D reconstruction of an astrocyte connectome (Fig. 1I–1K; Video S1; see Table S1 for the key characteristics of each of the three traced/reconstructed astrocytes).

Characterization of astrocyte branching architecture

In light and electron microscopy studies, protoplasmic astrocytes appear to possess a meshwork of small processes (Bushong *et al.*, 2002; Cali *et al.*, 2019; Gavrilov *et al.*, 2018; Ogata and Kosaka, 2002; Shigetomi *et al.*, 2013; Ventura and Harris, 1999); however, the intricate cellular architecture of astrocytes remains poorly understood. Additionally, whether astrocytes follow a tree-like dendritic architecture or establish a mesh-like spongiform morphology is an unresolved question (Rusakov, 2015).

To answer these questions, we used an “inside-out” sketching approach to trace the branching pattern of astrocytes from soma to the terminal processes and adopted the Root-Intermediate-Terminal (RIT) process labeling scheme, which was first used for dendritic arborization analysis (Uylings and van Pelt, 2002) (Fig. 2). Overall, this topography closely resembled what we observed in our 2D astrocyte traces (Fig. 2A1–2C1) and in our 3D reconstructions (Fig. 2A2–2C2). Using this organizational scheme, we defined a *root* process as a primary process that originates from the soma (Fig. 2A1–2A3). *Intermediate* processes are those that extend from the root processes and on certain occasions, extend to other intermediate processes (Fig. 2B1–2B3). Finally, we found that the small, thin *terminal* processes - defined as the processes that do not progress any further - extend non-selectively from the astrocytic soma, root, and intermediate processes (Fig. 2C1–2C3). Inside astrocytes, the abundance of terminal processes is one of the structural features accounting for a mesh-like, or spongiform, composition of astrocytes. The terminal processes also delineate the borders of astrocyte domains.

Although we followed the classic RIT labeling scheme to delineate astrocyte arborization, the resultant categorizations of astrocytic processes, i.e., root - intermediate - terminal processes, to some extent correspond well with a recently developed nomenclature system wherein the branch - branchlet - leaflet process terminology is alternatively used (Khakh and Sofroniew, 2015a) (Fig. 2A3–2B3–2C3–2F). Additionally, similar to leaflets - defined as the nanoscopic processes devoid of visible organelles (Chai *et al.*, 2017; Gavrilov *et al.*,

2018; Shigetomi *et al.*, 2013) - the terminal processes in our results are characterized by the absence of mitochondria (Fig. 2C3, Fig. 10E1). However, a major extension for the “leaflet” concept from the present study is the widespread sprout of leaflets from soma, branch, and branchlet (Fig. 2F).

Reflexive astrocyte processes and their structural support to neurites

Neurons typically display dendritic architecture, exhibiting tree-like arborization wherein different branches/processes do not self-connect or form loop-like structures. In contrast, early EM reconstruction showed that cultured astrocytes consist of processes that form connections within the same cell, termed reflexive contacts (Wolff *et al.*, 1998). While a spongiform morphology could be attributed to the extensive existence of the same loop-like processes (i.e., reflexive contacts) reported from the cultured astrocytes, this question has not been examined from EM specimens prepared from native protoplasmic astrocytes (Giaume *et al.*, 2010; Rusakov, 2015).

Our 2D traces and 3D reconstructions revealed that astrocyte processes make reflexive contacts within the same cell (Fig. 2D–2E). In the 2D traces, the tip of the reflexive process (whose originating, ‘parent’ process could be visually discerned), and the contact that it made with an adjacent membrane (from the same astrocyte) was further confirmed by the line analysis tool (see Methods). First, intermediate/branchlet processes could create reflexive contacts wherein two ‘daughter processes’ split at a branch point and then reconnect (Fig. 2D1–2D3). Further, thin terminal/leaflet processes that extended from an intermediate/branchlet process also created reflexive contacts by ‘looping’ around to contact the intermediate/branchlet process from which it originated (Fig. 2E1–2E3; Fig S3). Reflexive processes were widespread (Fig. S3) and therefore attributed to the second structural feature for a spongiform morphology of astrocytes.

It is interesting to note that these reflexive processes resemble the ‘O-ring’ structures observed in super-resolution imaging studies of hippocampal astrocytes (Arizono *et al.*, 2020; Panatier *et al.*, 2014); however, consistent with the definition for reflexive processes, the loop-like processes in our dataset were never completely fused; instead, they exhibited well-defined membrane borders (see Fig. 2D2, 2E2, and Fig. S3, in addition to the membrane borders depicted in yellow within the schematic in Fig. 2F; also see yellow reflexive contacts in Videos S2 and S3).

Astrocyte processes are extensively interwoven with surrounding neurites. To gain insight into the ultrastructural relationship between both cell types, we traced and reconstructed astrocytes in association with neural processes. We observed that a branchlet could enwrap an entire dendrite and then form a reflexive contact to allow the branchlet to further extend (Fig. 3A1–3A2; Video S2). Additionally, we observed that an astrocyte branch could enwrap axons, where it split in a similar manner and formed a reflexive contact around a bundle of axons (Fig. 3B1–3B2; Video S3). We also observed several examples of leaflets enwrapping neurites (such as the image shown in Fig. 2E). These observations underscore a classic notion that scaffolding structural support is a key function of astrocytes.

Ultrastructural visualization of inter-astrocyte contacts

Having characterized branching patterns *within* the same astrocyte, we next sought to examine the contact patterns *between* neighboring astrocytes. It is important to note that astrocytes are connected through an electrically low-resistance pathway (Kiyoshi and Zhou, 2019; Kuffler *et al.*, 1966) that is critical for coupled astrocytes to behave as an isopotential network (Huang *et al.*, 2018; Kiyoshi *et al.*, 2018; Ma *et al.*, 2016). However, the anatomical characteristics of astrocyte-astrocyte contacts have not yet been determined. Our "inside-out" tracing approach of three neighboring astrocytes enabled us to map, for the first time, the connectivity patterns between astrocytes (Fig. 4A). To begin, we found that a process extending from one astrocyte could contact more than one neighboring astrocyte (Fig. S4). We have also found that neighboring astrocytes established multiple contact sites with each other (Fig. 4). Inter-astrocytic contacts were mostly leaflet-leaflet contacts; among 15 contacts identified from our tracing, only one was leaflet-branchlet contact where the branchlet contained mitochondria (Fig. S5; and see File S3 for quantification of contact types). In contrast to an estimated 10% of overlapping of astrocytic domains revealed by confocal analysis (Bushong *et al.*, 2002), inter-astrocytic contacts were always located at the border of the domains at ultrastructural resolution (see yellow contacts in Fig. 4A). Of note, all the apparent leaflet-leaflet 'intrusion' in our presentations is purely an artifact resulting from the visual angle in which the interastrocytic leaflets exhibited a certain degree of overlap. Furthermore, close examination of astrocytic terminal processes revealed multiple types of contacts between astrocytes (Fig. 4B–D). We classified these contacts into two distinct categories: point-point contacts (Fig. 4B; Video S4) (7/15 contacts, 46.7%) and elongate contacts (Fig. 4C; Video S4) (8/15 contacts, 53.3%). Point-point contacts displayed a small surface area between the 'tips' of the terminal processes. Elongate contacts, on the other hand, showed a larger contact surface area. Presumably, these point-point and elongate contacts are the sites of gap junctional plaques (Nagy and Rash, 2000). However, while the nanoscopic processes can be readily resolved by SBF-SEM resolution (0.0077 μm/pixel), this technique is still below the limit to visualize individual gap junctions (Nielsen *et al.*, 2012).

Turning back to the idea of how low-resistance pathways are established, we found that many contact sites consisted of clusters of both point-point and elongate contacts. In one particular location, we observed astrocytes make six different contacts, and we termed this complex contact region as an astrocyte 'cluster of contacts' (Fig. 4D; Video S4). Within this connectome unit, multiple leaflets extended from branchlets in a fork-like manner (Fig. 4D). We hypothesized that the anatomical characteristics of 'cluster of contacts' serve as the inter-astrocytic electrical connectors that reduce the electrical resistance between astrocytes.

Computational modeling of the astrocyte connectome simulates a lowered pathway resistance

In our recently published reports (Kiyoshi *et al.*, 2018; Ma *et al.*, 2016), a high electrical coupling coefficient (CC, 94%) between astrocytes was revealed to account for astrocyte syncytial isopotentiality. Here, we used computational modeling to incorporate the ultrastructural anatomy of the reconstructed astrocyte connectome to simulate pathway resistance. In our model, each astrocyte in the syncytium is displayed as multiple

compartments, and in this multi-compartment representation, each astrocytic compartment is modeled as a passive cable (details are provided in the Methods, File S4, Tables S2 -S3, and Fig. S6).

We found a low CC of 47.28% in an inter-astrocyte pathway consisting of only a single point-point contact (Fig. S4C). A single elongate contact yields a higher CC at 82.05%, which is attributed to an increased number of likely gap junctions (Fig. S6D). Finally, the full cluster of six contacts increased the CC to 88.17% (Fig. S6E). Based on this, our computational model further predicts that 2, 3, and 4 connectome units can further increase the CC values to 92.5%, 93.92%, and 94.35%, respectively. Hence, the use of multiple contacts/contact types appears to be a biological design that reduces the electrical resistance between astrocytes (Kiyoshi and Zhou, 2019; Orkand *et al.*, 1966).

3D reconstruction of astrocytes in association with neurites

Astrocyte processes are extensively interwoven with surrounding neurites (Cali *et al.*, 2019; Gavrilov *et al.*, 2018; Kikuchi *et al.*, 2020; Ventura and Harris, 1999). Reconstruction of three astrocytes in association with neurites provided us with ultrastructural details of the anatomical relationships between both cell types (Fig. 5). We first traced (to completion) three dendrites and 920 axonal projections to all the identified spines that made synapses on these dendritic trees (Fig. 5C; Video S5). As noted in the Methods, we only traced a small number of neurites surrounding the three reconstructed astrocytes; many more neurites could be found within the EM field. To more easily view the dendritic spines, a small number of axons are depicted in Fig. S7A. Note the detailed structure of the dendritic spines shown in our reconstructions-representative of all six standard spine categories: thin, mushroom, stubby, cup, branched, and filopodia-like (Fig. S7B1–S7B6) (Hering and Sheng, 2001; Risher *et al.*, 2014). The three neurite reconstructions were then combined with the 3D reconstructions of the three astrocytes to generate a complete network-level view of the astrocyte-neurite interaction (Fig. 5D; Video S6).

Synapses make contact with all compartments of an astrocyte - from soma to leaflet processes

A prevailing view is that astrocytes interact with synapses at their terminal processes, or perisynaptic astrocyte processes (PAPs) (Gavrilov *et al.*, 2018; Peters *et al.*, 1976; Wolff *et al.*, 1998). While the structural aspects of PAPs tend to be more characteristic of leaflets, a recent report showed that synapses can contact a wide range of astrocytic processes (processes up to 800 nm in diameter) (Aboufares El Alaoui *et al.*, 2020). We sought to further examine this notion from our established astrocyte connectome. We found that every physical part of an astrocyte can make contact with synapses (Fig. 6A; see File S5 for quantification). 3D reconstructions of synapses (both pre-and post-synaptic elements) could be identified to abut the astrocyte soma (Fig. 6B1–6B2), branch (Fig. 6C1–6C2), branchlet (Fig. 6D1–6D2), leaflet (Fig. 6E1–6E2), reflexive processes (Fig. 6F1–6F2), and even astrocytic endfeet (Fig. 6G1–6G2). Quantitative analysis revealed further insight into the location-selectivity of synapses (Fig. 6H; $F_{(5, 43)} = 19.11$; $p < 0.0001$; See Table S4 for post-hoc analysis): there is a graded increase in the synapse density from soma to leaflets, and the highest density of synapses were found to abut leaflet and reflexive processes.

Importantly, our results indicate that all astrocyte compartments provide structural/functional support for synapses.

The majority of synapses make contact with astrocytic processes

Having established that all parts of an astrocyte can contact synapses (Fig. 6), we next examined the ultrastructural characteristics of these astrocyte-synapse contacts. Previous studies have reported that a large number of synapses make contact with astrocyte processes in the developing and mature rat cortex and hippocampus (Cali *et al.*, 2019; Kikuchi *et al.*, 2020; Ventura and Harris, 1999; Witcher *et al.*, 2007). However, in the mature mouse hippocampus, quantitative analysis of synapses with or without coverage from astrocytic processes was only reported from a 2D EM study, whereas the ultrastructural details, in terms of synapse-astrocyte contact patterns, remain unknown (Tanaka *et al.*, 2013). We approached these questions by using our three fully reconstructed neuronal dendrites and the axonal projections to their axon-spine interfaces (i.e., synapses) (presented in Fig. 5). In our 920 fully reconstructed synapses, each synapse was classified as 'asymmetric' (excitatory synapse) or 'symmetric' (inhibitory synapse) based on whether it exhibited a prominent or narrow postsynaptic density (Gray, 1959; Kikuchi *et al.*, 2020; Peters and Palay, 1996; Peters *et al.*, 1976; Santuy *et al.*, 2020) (see Fig. 7D1).

We next inspected and quantified the astrocytic processes that make contact at the synaptic cleft (Fig. 7A1–7A2), pre-or post-synaptic elements (Fig. 7B1–7B2), or the synapses devoid of contact with any astrocytic processes (Fig. 7C1–7C2) (see File S5 for quantification). First, we assessed the percentages of asymmetric versus symmetric synapses formed on the three dendritic trees (from Fig. 5). We found that most synapses were asymmetric (Fig. 7D2): 96% in dendrite-1 (226/235 synapses), 98% in dendrite-2 (226/231 synapses), and 98% in dendrite-3 (444/454 synapses) (Fig. 7D2).

We then examined the patterns of synapse-astrocyte contacts from 920 synapses. First, independent of asymmetric or symmetric subtypes of synapses, 86% of synapses received coverage from astrocytic processes. Second, in both asymmetric and symmetric synapses, "cleft contact" was found to be the dominant type of synapse-astrocyte contact (~60%), followed by a pattern with partial coverage of pre-or-post synaptic elements by astrocytes (>25%) (Fig. 7E). However, there were also quantitative differences when considering asymmetric and symmetric as different types of synapses observed in the patterns of synapse-astrocyte contacts (Fig. 7E; $F_{(5, 12)} = 54.96$; $p < 0.0001$; one-way ANOVA. See Table S5 for post-hoc analysis). Specifically, out of the 920 total synapses, ~57% of asymmetric synapses (Fig. 7E; solid green bar), and ~1.5% of symmetric synapses (Fig. 7E; patterned green bar), respectively, contacted astrocytes at the cleft. Further, another 26% of synapses in the asymmetric class (Fig. 7E; solid orange bar), and 1% of synapses in the symmetric class (Fig. 7E; patterned orange bar), respectively, had pre-or post-synaptic contact with astrocytes. In contrast, 14% of synapses in the asymmetric class (Fig. 7E; solid purple bar), and <1% of synapses in the symmetric class (Fig. 7E; patterned purple bar), respectively, had no contact with astrocytes. Taken together, these results indicate that 86% of synapses have contact with astrocyte processes, and most of these astrocyte-synapse contacts occur at the synaptic cleft (compared to pre and/or postsynaptic elements).

Neighboring astrocytes can share coverage of a single synapse

Domain exclusivity of synaptic coverage has previously been proposed (Halassa *et al.*, 2007). Now, the interfaces reconstructed from our three neighboring astrocytes offer a unique opportunity to examine this notion further. We found that a synapse can receive synaptic coverage by two neighboring astrocytes (Fig. 8; Video S7). Note that on each side of the synapse, a different astrocyte process (pink or blue) is adjacent to the synaptic cleft (Fig. 8A–8B; Video S7). This coverage persisted across a significant portion of the synaptic cleft, and while it continued across multiple z-planes, it simultaneously formed contacts with the other astrocyte process (Fig. 8A; Video S7). These results suggest that the interaction of a given synapse with an astrocytic process is not restricted within a domain. Functionally, this indicates that different astrocytes can provide similar structural/functional support, such as neurotransmitter uptake, to the same synapse.

Paucity of vesicle-like structures in astrocyte processes adjacent to synapses

Calcium-dependent vesicular release of gliotransmitters has been shown to modulate synaptic transmission and plasticity (Araque *et al.*, 1999; Perea *et al.*, 2009). Our extensive tracing of synapse-astrocyte contacts provided the opportunity for examination of the location and quantity of intracellular vesicle-like structures in astrocytes.

To begin, we traced and used the characteristic presynaptic ‘vesicle-like organelles’ as a reference/control (see Fig. 9A; for a description of criteria used to define these structures, see Fig. S2). Then, structures (within astrocytes) that had the same appearance as vesicles within the presynaptic buttons were considered as ‘vesicle-like’ organelles. With these criteria in mind, we examined every compartment inside astrocytic domains, given that each process type exhibited direct association with synapses (Fig. 6). Across astrocyte process types, we observed only a paucity of vesicle-like structures positioned adjacent to synapses, in contrast to the massive assembly of vesicles noted in the presynaptic boutons (Fig. 9A–9F). In addition to the lack of an appreciable collection of vesicle-like structures in astrocyte processes adjacent to synapses, vesicle-like structures were also sparse in other regions of the astrocyte (see arrowheads in Fig. 9B, 9C, and 9E). Quantitative analysis showed that, in contrast to a high density of ~612 vesicles/μm^3 in presynaptic buttons, only ~2 vesicle-like structures/μm^3 were observed across all compartments of the astrocytes, with no significant difference in number between astrocyte process types (Fig. 9G; $F_{(4, 39)} = 0.816$; $p = 0.523$; one-way ANOVA and see File S7). Together, the lack of vesicle-like structures in astrocytes suggests that if gliotransmission occurs, it is unlikely mediated through a Ca^{2+}-dependent vesicular-release mechanism that is used by neurons.

Abundance of mitochondria within astrocytes

Our reconstructions of three astrocytes enabled us to ascertain the location and quantity of mitochondria within this glial subtype. To begin, we first traced all mitochondria found within the three astrocytes (see Fig. S2 for a description about 2D EM mitochondria identification and see Fig. S8 for a representation of reconstructed mitochondria within one of the astrocytes). Our reconstructions revealed that, with an exception of absence of mitochondria in leaflets, mitochondria establish a dense tubular network running from soma to branchlets, including the end-foot processes that enwrap blood vessels (Fig. S9;

Fig. 10A–10G). Interestingly, our quantitative analysis showed that the average diameter of leaflets, 123.83 μm, is at least two times smaller than the tubular diameter of mitochondria, 300.41 μm (Fig. 10H; $t_{(148)} = 22.71$; $p < 0.0001$; unpaired t-test and see File S8), indicating that lack of mitochondria in leaflets is simply due to space constraint within these fine, terminal processes.

Given the abundant presence of mitochondria network within astrocytes, we next sought to determine whether electrically silent astrocytes (perceived to be energy-saving cells) contain a comparable amount of mitochondria as excitable neurons. To answer this question, we first traced all mitochondria found throughout each of our three reconstructed dendrites, in addition to the mitochondria located within the axons associated with each dendrite (Fig. 11A and see Fig. S10 for the mitochondrial network of neurites). A magnified view of mitochondria (yellow) found within astrocytes, axons, and dendrites are depicted in Fig. 11B–11D. Quantification of the mitochondria volume to cellular compartment volume revealed that the average mitochondria volume ratio in astrocytes (10.40%) is comparable to that of dendrites (5.14%) and axons (4.61%) with no statistical difference observed (Fig. 11E; $F_{(2, 6)} = 0.646$; $p = 0.053$; One-way ANOVA and see file S9). These observations show the mitochondria in astrocytes are comparable in abundance to those in excitable neurons.

Discussion:

In the emerging field of structural and functional connectomics (Alivisatos *et al.*, 2012; Fornito *et al.*, 2015; Swanson and Lichtman, 2016), the ultrastructural connectivity of neurons has been highlighted in several recent studies (Kasthuri *et al.*, 2015; Mishchenko *et al.*, 2010). In the present study, we've taken advantage of an *Aldh1l1*-eGFP reporter mouse for pre-identification of neighboring astrocytes in EM specimen preparation and SBF-SEM for preserving the nanoscopic astrocytic processes and intracellular structures to create the first ultrastructural view of an astrocyte connectome. Here, significant insights have been provided concerning the structural complexity of astrocyte processes, the structural astrocyte-astrocyte and astrocyte-synapse interactions, and the spatial location and quantity of vesicle-like structures and mitochondria inside astrocytes and neurons.

Complexity of astrocyte processes: spongiform morphology and neurite structural support

With respect to the arborization patterning, we found that astrocyte processes generally follow a Branch-Branchlet-Leaflet scheme (Gavrilov *et al.*, 2018; Khakh and Sofroniew, 2015a), which closely resembles dendritic topology that has been previously reported (Uylings and van Pelt, 2002). Notably, we also observed two distinct patterning features. First, numerous leaflet/terminal processes extend out from every part of the astrocyte. We also observed an abundance of reflexive, loop-like structures. Although technical limitations precluded us from validating that these self-connecting structures contain gap junctions, other studies have confirmed the existence of gap junctions in such reflexive contacts (Nagy *et al.*, 1997; Wolff *et al.*, 1998). These two features together give rise to spongiform morphology by which a large surface-to-volume ratio (~26 μm^3) can be generated for

astrocytes to functionally interact with other CNS constituents - namely synapses and vasculature (Hama *et al.*, 2004; Semyanov and Verkhratsky, 2021).

The significant number of reflexive processes raises interesting questions about their functional contribution. We found that reflexive processes always 'wrap around' axonal and dendritic components, indicative of their robust structural support role for neurites. Interestingly, we noted a wide range of axons (varying from a single axon to bundles of 10+ axons) capable of being enwrapped by an astrocyte reflexive process. Furthermore, we observed a reflexive process enwrap a dendrite that was approximately 6 times the diameter of an average axon (see Fig 3A), which may indicate a large structural 'capacity' for astrocytes to enwrap any size axonal/dendritic structures. In addition, these loop-like structures underlie a major structural basis of astrocytes, helping to create a large surface area-to-volume ratio so that astrocyte processes can interact with more synapses. This view is supported by our observation that reflexive astrocyte processes accommodate the second most synapses (with ~0.95 synapses per unit area) compared to all other astrocyte process types. This unique ability for astrocytes to loop around neurites may provide structural fluidity, such that astrocytes can accommodate and support existing synapses. Along these lines, a recent super-resolution imaging study revealed the existence of numerous similar 'loop-like' structures in the meshwork of astrocytic processes, termed 'nodes' (Arizono *et al.*, 2020). The similarity of "nodes" (revealed at 50 nm resolution in the Arizono et al study) to the reflexive processes (revealed at 7.7 nm EM resolution in our study) suggests they most likely represent the same structural elements of astrocyte processes. Interestingly, "nodes" are the sites of initiation of calcium signals. Indeed, calcium activity at the nodes positively correlated with dendritic spine size, suggesting that neuronal transmitter-initiated astrocytic Ca^{2+} signaling maintains and regulates the structure of synapses. Notably, however, the induction of long-term potentiation, a synaptic memory mechanism, triggers the withdrawal of astrocytic processes from those active synapses for facilitation of inter-synaptic crosstalk (Henneberger *et al.*, 2020). Hence, the regulation of synaptic plasticity (mediated in part to the close interaction between astrocytes and synapses), is likely very complex.

Ultrastructural view of inter-astrocyte contacts and their functional implications

The idea that low-resistance pathways exist between astrocytes was first discovered over 50 years ago in mudpuppy optic nerves (Kuffler *et al.*, 1966). Recently, a gap junction mediated low inter-astrocyte electrical resistance was directly demonstrated in rodents to serve as the *biophysical* basis for a phenomenon termed syncytial isopotentiality (Kiyoshi *et al.*, 2018; Ma *et al.*, 2016). However, until now, the *anatomical* basis underlying the low resistance pathway between astrocytes was not known.

Our data confirmed that astrocyte-astrocyte contacts mostly occur between leaflets protruding from branchlets, which ultimately form the interface of astrocytic domains (Bushong *et al.*, 2002; Ogata and Kosaka, 2002) (Fig. 4). Further, the ultrastructural details of two major inter-astrocytic contact types (point-point and elongate) were revealed in our study. Analysis of these contacts allowed us to rationalize that contacts at the interface between two astrocytes function as 'electrical connectors' to decrease the resistance between two astrocytes (Kuffler *et al.*, 1966).

Biophysically, the reflexive loops should be another mechanism by which the astrocyte is able to lower its overall resistance. We should note that the abundance of reflexive loops and the structural variability of these loops made their quantification difficult; hence, our mathematical simulations were made without the consideration of reflexive terminal processes. An additional limitation of our simplistic computational model is that we did not correlate gap junction coupling strength with changes in astrocytic cell conductance or input resistance - both of which are factors that can influence overall pathway resistance (Stephan *et al.*, 2021; Zhou *et al.*, 2021).

While our current study did not elucidate the functional significance of the various types of astrocyte contacts, the assembly of astrocytes into a low-resistance syncytium raises the question as to whether this anatomical design endows astrocytes the ability to more closely associate with synapses to modulate brain function. Along these lines, the conductivity of gap junctions can be regulated through various signaling pathways as a result of neurotransmitter release and pH or temperature change (Bukauskas and Verselis, 2004; Goodenough and Paul, 2009), raising the prospect that neurotransmission can enhance or weaken coupling within a given cluster of contacts. Hence, at any given time, certain clusters within an interface may undergo strengthening while other units may weaken. As a result, syncytial isopotentiality is a spatiotemporal summation of all events occurring across the clusters, and it is likely influenced by the proximity of astrocytes and synapses (a topic discussed below).

Ultrastructural view of synapse-astrocyte contacts

By tracing the projections of 920 axons (to the entire population of spines) located on three reconstructed dendritic trees, we show that ~86% of synapses on these dendritic trees are contacted by astrocytes in the adult mouse hippocampus. Notably, this percentage of synapse coverage is higher than those synapses examined from the developing rat somatosensory cortex (68% coverage) (Kikuchi *et al.*, 2020). It is also higher than the synapses in mature rat and mouse stratum radiatum (57%, 62%, and ~45% coverage, respectively) (Tanaka *et al.*, 2013; Ventura and Harris, 1999; Witcher *et al.*, 2007). Differences in the brain region, developmental stage, and/or analysis methods likely contributed to a higher percentage of astrocyte-covered synapses that we observed.

Further, our finding that a majority of astrocyte-synapse contacts occurred to the axon-spine interface (cleft), compared to post- or pre-synaptic elements, is in agreement with previous studies in both the developing (Kikuchi *et al.*, 2020) and mature brain (Witcher *et al.*, 2007). Of note, whereas most asymmetric synapses are excitatory, symmetric synapses are inhibitory (Peters and Palay, 1996). Interestingly, ~94% of all synapses reported in the P14 developing brain (Kikuchi *et al.*, 2020) were asymmetric, a finding that we also observed in our study in the mature (P45) brain, suggesting that the instructive role of astrocytes in synaptogenesis occurs mainly in the developing brain (Allen and Eroglu, 2017). However, here we should note that our retrograde tracing of axons (from the dendritic spine outward) likely precluded us from tracing inhibitory axonal projections onto the dendritic shafts (Tanaka et al., 2013). Hence, our analysis did not include those synapses that contacted the dendrite shaft.

In terms of location-selectivity of astrocyte-synapse interaction, a prevailing view is that astrocyte leaflets preferentially contact synapses (Gavrilov *et al.*, 2018; Patrushev *et al.*, 2013); these leaflets provide structural support, clear neurotransmitters from the synaptic cleft, and respond to local synaptic activity via the release of gliotransmitters (Araque *et al.*, 2014; Gavrilov *et al.*, 2018; Papouin *et al.*, 2017). Hence, leaflets are considered as the third anatomical/functional component in the 'tripartite synapse' (Araque *et al.*, 1999). While the density of synapses surrounding leaflets was high, we also found a "non-discriminatory" location selectivity of synapses abutting all other astrocytic cellular compartments, suggesting that synaptic support machinery is uniformly equipped throughout the entire astrocyte.

Although it remains unknown as to why synapses interact with leaflets more so than they do with other astrocyte processes, we found that leaflets extend from each astrocytic compartment (i.e., from soma to branchlets); thus, more frequent contact of leaflets with synapses is unlikely due to their location within an astrocyte domain. A plausible interpretation would be that leaflets are more dynamic processes induced by more active regional neuronal signaling. Along these lines, it has been shown that the neuronal BDNF signal to an astrocytic TrKB.T1 receptor is required for the induction of leaflets (Holt *et al.*, 2019). Similarly, some of the reflexive processes (which also contact a very large number of synapses) could also be induced through similar signaling pathways.

In our 3D reconstructions of network-level astrocyte-synapse contacts, we observed synapses being touched by more than one astrocyte. Although tracing limitations precluded us from quantifying the fraction of total synapses contacted by more than one astrocyte, this observation provides clear anatomical evidence that synaptic coverage does not occur exclusively within one astrocyte domain - a finding that was also observed using multi-color electron microscopy (Adams *et al.*, 2016). These results also suggest that astrocytes within a given region are unlikely to be functionally specialized.

Paucity of vesicle-like structures within astrocytes

The fact that astrocytes contact synapses is central to the highly debated topic of gliotransmission (Fiacco and McCarthy, 2018; Savtchouk and Volterra, 2018), wherein astrocytes modulate synaptic transmission via Ca^{2+}-dependent vesicular release of 'gliotransmitters' (i.e., neurotransmitters, ATP, glutamate and D-serine). However, we could only find a few vesicular-like structures located in astrocytes. Furthermore, the few organelles that we could detect did not always abut synapses, nor were they located specifically within leaflets (i.e., we observed a small quantity in the astrocyte soma, branch, and branchlet processes too). This lack of vesicular-like structures throughout the entirety of the astrocyte is in agreement with a recently published study reporting that astrocyte processes do not contain structures similar to neurotransmitter vesicles (Chai *et al.*, 2017). However, it is important to note that while the quantity of these vesicle-like structures observed within astrocytes in our study (and in others) is small, this is only a problem if it is assumed that the gliotransmitter release in astrocytes must follow the same Ca^{2+} -dependent vesicular release mechanism in neurons. Hence, caution should be taken when considering this paucity of astrocyte vesicle-like structures as clear evidence against gliotransmission.

Further, we should note that the resolution of our EM study did not allow us to discern the specific shape of vesicle-like structures that could potentially differentiate glutamatergic versus GABAergic synapses. Hence, our identification of astrocytic vesicle-like structures was solely made according to shape, size, and electron density when compared to neuronal presynaptic vesicles.

Abundance of mitochondria within astrocytes

Through tracing and reconstruction of mitochondria from 3 neighboring astrocytes, here, we provide the first and complete ultrastructural view of a mitochondria network in astrocytes (Fig. 10, Fig. 11; Video S8). We noted an abundance of mitochondria distributed in various astrocyte compartments from soma, branch, branchlet, and endfeet, to non-leaflet reflexive processes.

Interestingly, we found that while fine astrocytic leaflets contain other subcellular structures (such as ER, glycogen granules, and vesicle-like organelles), they are completely devoid of mitochondria (Fig. 10E), which is consistent with several other studies (Aboufares El Alaoui *et al.*, 2020; Gavrilov *et al.*, 2018; Patrushev *et al.*, 2013). Many studies have shown that calcium generation via this internal storage route is one of the critical mechanisms underlying astrocyte-neuron communication (Agarwal *et al.*, 2017; Li and Rinzel, 1994; Sherwood *et al.*, 2017; Ullah *et al.*, 2006). Notably, because these leaflets lack calcium-release organelles, mitochondria, and endoplasmic reticulum (ER), they are not able to release calcium to allow for Ca^{2+}-dependent astrocyte-neuron communication (Agarwal *et al.*, 2017; Li and Rinzel, 1994; Sherwood *et al.*, 2017). Hence, these astrocytic leaflets would depend on the calcium transients generated from upstream organelle-containing processes to modulate synaptic transmission and plasticity (Fig. 10D). It is also interesting to note that numerous synapses are associated with mitochondria-containing processes (Fig. 6), implying astrocytic processes may vary in their capacity to influence synaptic function.

With respect to the quantity of mitochondria, we were somewhat surprised to note its abundance within astrocytes. Along these lines, previous studies have shown that much (~75–80%) of the oxidative energy in the brain is utilized by synapses for signaling function (Attwell and Laughlin, 2001; Hyder *et al.*, 2013; Riveros *et al.*, 1986; Wong-Riley *et al.*, 1989). On the other hand, only ~5–15% of the ATP expenditure in the brain is thought to account for metabolic processes within astrocytes (Attwell and Laughlin, 2001; Belanger *et al.*, 2011). However, the mitochondria to astrocyte volume ratio is comparable to the mitochondria to neurite (i.e., axon and dendrite) volume ratio (Fig. 11E), suggesting that astrocytic homeostatic and synaptic support functions in the brain would be rather energy-demanding processes that may have been overlooked in the past. Hence, future studies would be crucial in defining the role of mitochondria in astrocyte bioenergetics, as well as other roles related to calcium signaling in physiological processes and apoptotic cell death in pathological contexts.

Supplementary Material

Refer to Web version on PubMed Central for supplementary material.

Acknowledgements:

The authors thank Dr. Thomas Südhof for his suggestions regarding the representation of Figure 1. The authors would also like to thank Dr. Corrado Cali for his advice regarding the ellipsoid model for calculation of the percentage of astrocyte(s) reconstructed within the EM tissue block.

Funding:

This work was sponsored by grants from National Institute of Neurological Disorders and Stroke; Grant code: RO1NS062784, R56NS097972, RO1NS116059 (MZ), National Science Foundation; Grant Code: DMS1410935 (DT), and an Alumni Grants for Graduate Research and Scholarship (AGGRS) and Distinguished University Fellowship, Ohio State University (to SA).

Data Availability Statement:

All data can be found within the main manuscript text or within supplementary files. The full EM Reconstruct files (i.e., tracings) will be deposited in a public repository upon acceptance of the manuscript.

References

Aboufares El Alaoui A, Jackson M, Fabri M, de Vivo L, Bellesi M, 2020. Characterization of Subcellular Organelles in Cortical Perisynaptic Astrocytes. Front Cell Neurosci 14, 573944. [PubMed: 33633542]

Adams SR, Mackey MR, Ramachandra R, Palida Lemieux SF, Steinbach P, Bushong EA, Butko MT, Giepmans BNG, Ellisman MH, Tsien RY, 2016. Multicolor Electron Microscopy for Simultaneous Visualization of Multiple Molecular Species. Cell Chem Biol 23, 1417–1427. [PubMed: 27818300]

Agarwal A, Wu PH, Hughes EG, Fukaya M, Tischfield MA, Langseth AJ, Wirtz D, Bergles DE, 2017. Transient Opening of the Mitochondrial Permeability Transition Pore Induces Microdomain Calcium Transients in Astrocyte Processes. Neuron 93, 587–605 e587. [PubMed: 28132831]

Alivisatos AP, Chun M, Church GM, Greenspan RJ, Roukes ML, Yuste R, 2012. The brain activity map project and the challenge of functional connectomics. Neuron 74, 970–74. [PubMed: 22726828]

Allen NJ, Eroglu C, 2017. Cell Biology of Astrocyte-Synapse Interactions. Neuron 96, 697–708. [PubMed: 29096081]

Araque A, Carmignoto G, Haydon PG, Oliet SH, Robitaille R, Volterra A, 2014. Gliotransmitters travel in time and space. Neuron 81, 728–739. [PubMed: 24559669]

Araque A, Parpura V, Sanzgiri RP, Haydon PG, 1999. Tripartite synapses: glia, the unacknowledged partner. Trends Neurosci 22, 208–215. [PubMed: 10322493]

Arizono M, Inavalli V, Panatier A, Pfeiffer T, Angibaud J, Levet F, Ter Veer MJT, Stobart J, Bellocchio L, Mikoshiba K, Marsicano G, Weber B, Oliet SHR, Nagerl UV, 2020. Structural basis of astrocytic Ca(2+) signals at tripartite synapses. Nature communications 11, 1906.

Attwell D, Laughlin SB, 2001. An energy budget for signaling in the grey matter of the brain. J Cereb Blood Flow Metab 21, 1133–1145. [PubMed: 11598490]

Belanger M, Allaman I, Magistretti PJ, 2011. Brain energy metabolism: focus on astrocyte-neuron metabolic cooperation. Cell Metab 14, 724–738. [PubMed: 22152301]

Bergles DE, Roberts JD, Somogyi P, Jahr CE, 2000. Glutamatergic synapses on oligodendrocyte precursor cells in the hippocampus. Nature 405, 187–191. [PubMed: 10821275]

Bukauskas FF, Verselis VK, 2004. Gap junction channel gating. Biochim Biophys Acta 1662, 42–60. [PubMed: 15033578]

Bushong EA, Martone ME, Jones YZ, Ellisman MH, 2002. Protoplasmic astrocytes in CA1 stratum radiatum occupy separate anatomical domains. J Neurosci 22, 183–192. [PubMed: 11756501]

Cali C, Agus M, Kare K, Boges DJ, Lehvaslaiho H, Hadwiger M, Magistretti PJ, 2019. 3D cellular reconstruction of cortical glia and parenchymal morphometric analysis from Serial Block-Face Electron Microscopy of juvenile rat. Prog Neurobiol 183, 101696. [PubMed: 31550514]

Cali C, Baghabra J, Boges DJ, Holst GR, Kreshuk A, Hamprecht FA, Srinivasan M, Lehvaslaiho H, Magistretti PJ, 2016. Three-dimensional immersive virtual reality for studying cellular compartments in 3D models from EM preparations of neural tissues. J Comp Neurol 524, 23–38. [PubMed: 26179415]

Chai H, Diaz-Castro B, Shigetomi E, Monte E, Octeau JC, Yu X, Cohn W, Rajendran PS, Vondriska TM, Whitelegge JP, Coppola G, Khakh BS, 2017. Neural Circuit-Specialized Astrocytes: Transcriptomic, Proteomic, Morphological, and Functional Evidence. Neuron 95, 531–549 e539. [PubMed: 28712653]

Denk W, Horstmann H, 2004. Serial block-face scanning electron microscopy to reconstruct three-dimensional tissue nanostructure. PLoS biology 2, e329. [PubMed: 15514700]

Ermentrout B, Terman D, 2010. Mathematical Foundations of Neuroscience. book published by Springer, 2010.

Fiacco TA, McCarthy KD, 2018. Multiple Lines of Evidence Indicate That Gliotransmission Does Not Occur under Physiological Conditions. J Neurosci 38, 3–13. [PubMed: 29298904]

Fiala JC, 2005. Reconstruct: a free editor for serial section microscopy. J Microsc 218, 52–61. [PubMed: 15817063]

Fornito A, Zalesky A, Breakspear M, 2015. The connectomics of brain disorders. Nat Rev Neurosci 16, 159–172. [PubMed: 25697159]

Gavrilov N, Golyagina I, Brazhe A, Scimemi A, Turlapov V, Semyanov A, 2018. Astrocytic Coverage of Dendritic Spines, Dendritic Shafts, and Axonal Boutons in Hippocampal Neuropil. Front Cell Neurosci 12, 248. [PubMed: 30174590]

Giaume C, Koulakoff A, Roux L, Holcman D, Rouach N, 2010. Astroglial networks: a step further in neuroglial and gliovascular interactions. Nat Rev Neurosci 11, 87–99. [PubMed: 20087359]

Goodenough DA, Paul DL, 2009. Gap junctions. Cold Spring Harbor perspectives in biology 1, a002576. [PubMed: 20066080]

Gray EG, 1959. Electron microscopy of synaptic contacts on dendrite spines of the cerebral cortex. Nature 183, 1592–1593. [PubMed: 13666826]

Gutnick MJ, Connors BW, Ransom BR, 1981. Dye-coupling between glial cells in the guinea pig neocortical slice. Brain Res 213, 486–492. [PubMed: 7248773]

Halassa MM, Fellin T, Takano H, Dong JH, Haydon PG, 2007. Synaptic islands defined by the territory of a single astrocyte. J Neurosci 27, 6473–6477. [PubMed: 17567808]

Hama K, Arii T, Katayama E, Marton M, Ellisman MH, 2004. Tri-dimensional morphometric analysis of astrocytic processes with high voltage electron microscopy of thick Golgi preparations. Journal of neurocytology 33, 277–285. [PubMed: 15475683]

Henneberger C, Bard L, Panatier A, Reynolds JP, Kopach O, Medvedev NI, Minge D, Herde MK, Anders S, Kraev I, Heller JP, Rama S, Zheng K, Jensen TP, Sanchez-Romero I, Jackson CJ, Janovjak H, Ottersen OP, Nagelhus EA, Oliet SHR, Stewart MG, Nagerl UV, Rusakov DA, 2020. LTP Induction Boosts Glutamate Spillover by Driving Withdrawal of Perisynaptic Astroglia. Neuron 108, 919–936 e911. [PubMed: 32976770]

Hering H, Sheng M, 2001. Dendritic spines: structure, dynamics and regulation. Nat Rev Neurosci 2, 880–888. [PubMed: 11733795]

Hillman H, Deutsch K, 1978. Area changes in slices of rat brain during preparation for histology or electron microscopy. J Microsc 114, 77–84. [PubMed: 361964]

Holt LM, Hernandez RD, Pacheco NL, Torres Ceja B, Hossain M, Olsen ML, 2019. Astrocyte morphogenesis is dependent on BDNF signaling via astrocytic TrkB.T1. eLife 8.

Huang M, Du Y, Kiyoshi CM, Wu X, Askwith CC, McTigue DM, Zhou M, 2018. Syncytial Isopotentiality: An Electrical Feature of Spinal Cord Astrocyte Networks. Neuroglia 1, 271–279.

Hyder F, Fulbright RK, Shulman RG, Rothman DL, 2013. Glutamatergic function in the resting awake human brain is supported by uniformly high oxidative energy. J Cereb Blood Flow Metab 33, 339–347. [PubMed: 23299240]

Kalimo H, 1976. The role of the blood-brain barrier in perfusion fixation of the brain for electron microscopy. Histochem J 8, 1–12. [PubMed: 1270329]

Kasthuri N, Hayworth KJ, Berger DR, Schalek RL, Conchello JA, Knowles-Barley S, Lee D, Vazquez-Reina A, Kaynig V, Jones TR, Roberts M, Morgan JL, Tapia JC, Seung HS, Roncal WG, Vogelstein JT, Burns R, Sussman DL, Priebe CE, Pfister H, Lichtman JW, 2015. Saturated Reconstruction of a Volume of Neocortex. Cell 162, 648–661. [PubMed: 26232230]

Khakh BS, Sofroniew MV, 2015a. Diversity of astrocyte functions and phenotypes in neural circuits. Nat Neurosci 18, 942–952. [PubMed: 26108722]

Khakh BS, Sofroniew MV, 2015b. Diversity of astrocyte functions and phenotypes in neural circuits. Nature Neuroscience 18, 942–952. [PubMed: 26108722]

Kikuchi T, Gonzalez-Soriano J, Kastanauskaite A, Benavides-Piccione R, Merchan-Perez A, DeFelipe J, Blazquez-Llorca L, 2020. Volume Electron Microscopy Study of the Relationship Between Synapses and Astrocytes in the Developing Rat Somatosensory Cortex. Cereb Cortex 30, 3800–3819. [PubMed: 31989178]

Kiyoshi CM, Du Y, Zhong S, Wang W, Taylor AT, Xiong B, Ma B, Terman D, Zhou M, 2018. Syncytial isopotentiality: A system-wide electrical feature of astrocytic networks in the brain. Glia 66, 2756–2769. [PubMed: 30277621]

Kiyoshi CM, Zhou M, 2019. Astrocyte syncytium: a functional reticular system in the brain. Neural regeneration research 14, 595–596. [PubMed: 30632498]

Korogod N, Petersen CC, Knott GW, 2015. Ultrastructural analysis of adult mouse neocortex comparing aldehyde perfusion with cryo fixation. eLife 4.

Kuffler SW, Nicholls JG, Orkand RK, 1966. Physiological properties of glial cells in the central nervous system of amphibia. J Neurophysiol 29, 768–787. [PubMed: 5966434]

Li YX, Rinzel J, 1994. Equations for InsP3 receptor-mediated [Ca2+]i oscillations derived from a detailed kinetic model: a Hodgkin-Huxley like formalism. Journal of theoretical biology 166, 461–473. [PubMed: 8176949]

Lovatt D, Sonnewald U, Waagepetersen HS, Schousboe A, He W, Lin JH, Han X, Takano T, Wang S, Sim FJ, Goldman SA, Nedergaard M, 2007. The transcriptome and metabolic gene signature of protoplasmic astrocytes in the adult murine cortex. J Neurosci 27, 12255–12266. [PubMed: 17989291]

Ma B, Buckalew R, Du Y, Kiyoshi CM, Alford CC, Wang W, McTigue DM, Enyeart JJ, Terman D, Zhou M, 2016. Gap junction coupling confers isopotentiality on astrocyte syncytium. Glia 64, 214–226. [PubMed: 26435164]

Medvedev N, Popov V, Henneberger C, Kraev I, Rusakov DA, Stewart MG, 2014. Glia selectively approach synapses on thin dendritic spines. Philosophical transactions of the Royal Society of London. Series B, Biological sciences 369, 20140047. [PubMed: 25225105]

Mishchenko Y, Hu T, Spacek J, Mendenhall J, Harris KM, Chklovskii DB, 2010. Ultrastructural analysis of hippocampal neuropil from the connectomics perspective. Neuron 67, 1009–1020. [PubMed: 20869597]

Muller CM, 1996. Gap-junctional communication in mammalian cortical astrocytes: development, modifiability and possible functions. *In:* Gap Junctions in the nervous system *Editors:* Spary DC, Dermietzel R. Austin, TX: RG Landes Company Chapter 12, pp.203–212.

Nagy JI, Ochalski PA, Li J, Hertzberg EL, 1997. Evidence for the co-localization of another connexin with connexin-43 at astrocytic gap junctions in rat brain. Neuroscience 78, 533–548. [PubMed: 9145808]

Nagy JI, Rash JE, 2000. Connexins and gap junctions of astrocytes and oligodendrocytes in the CNS. Brain Res Brain Res Rev 32, 29–44. [PubMed: 10751655]

Nagy JI, Rash JE, 2003. Astrocyte and oligodendrocyte connexins of the glial syncytium in relation to astrocyte anatomical domains and spatial buffering. Cell Commun Adhes 10, 401–406. [PubMed: 14681048]

Nielsen MS, Axelsen LN, Sorgen PL, Verma V, Delmar M, Holstein-Rathlou NH, 2012. Gap junctions. Compr Physiol 2, 1981–2035. [PubMed: 23723031]

Ogata K, Kosaka T, 2002. Structural and quantitative analysis of astrocytes in the mouse hippocampus. Neuroscience 113, 221–233. [PubMed: 12123700]

Orkand RK, Nicholls JG, Kuffler SW, 1966. Effect of nerve impulses on the membrane potential of glial cells in the central nervous system of amphibia. J Neurophysiol 29, 788–806. [PubMed: 5966435]

Panatier A, Arizono M, Nagerl UV, 2014. Dissecting tripartite synapses with STED microscopy. Philosophical transactions of the Royal Society of London. Series B, Biological sciences 369, 20130597. [PubMed: 25225091]

Papouin T, Dunphy J, Tolman M, Foley JC, Haydon PG, 2017. Astrocytic control of synaptic function. Philosophical transactions of the Royal Society of London. Series B, Biological sciences 372.

Pascual O, Casper KB, Kubera C, Zhang J, Revilla-Sanchez R, Sul JY, Takano H, Moss SJ, McCarthy K, Haydon PG, 2005. Astrocytic purinergic signaling coordinates synaptic networks. Science 310, 113–116. [PubMed: 16210541]

Patrushev I, Gavrilov N, Turlapov V, Semyanov A, 2013. Subcellular location of astrocytic calcium stores favors extrasynaptic neuron-astrocyte communication. Cell calcium 54, 343–349. [PubMed: 24035346]

Perea G, Araque A, 2007. Astrocytes potentiate transmitter release at single hippocampal synapses. Science 317, 1083–1086. [PubMed: 17717185]

Perea G, Navarrete M, Araque A, 2009. Tripartite synapses: astrocytes process and control synaptic information. Trends Neurosci 32, 421–431. [PubMed: 19615761]

Peters A, Palay SL, 1996. The morphology of synapses. Journal of neurocytology 25, 687–700. [PubMed: 9023718]

Peters A, Palay SL, Webster HD, 1976. The fine structure of the nervous system: the neurons and supporting cells 395 pp, W.B. Saunders Company, Philadelphia.

Rash JE, Yasumura T, Davidson KG, Furman CS, Dudek FE, Nagy JI, 2001a. Identification of cells expressing Cx43, Cx30, Cx26, Cx32 and Cx36 in gap junctions of rat brain and spinal cord. Cell Commun Adhes 8, 315–320. [PubMed: 12064610]

Rash JE, Yasumura T, Dudek FE, Nagy JI, 2001b. Cell-specific expression of connexins and evidence of restricted gap junctional coupling between glial cells and between neurons. J Neurosci 21, 1983–2000. [PubMed: 11245683]

Risher WC, Ustunkaya T, Singh Alvarado J, Eroglu C, 2014. Rapid Golgi analysis method for efficient and unbiased classification of dendritic spines. PLoS One 9, e107591. [PubMed: 25208214]

Riveros N, Fiedler J, Lagos N, Munoz C, Orrego F, 1986. Glutamate in rat brain cortex synaptic vesicles: influence of the vesicle isolation procedure. Brain Res 386, 405–408. [PubMed: 2877717]

Rose CR, Chatton JY, 2016. Astrocyte sodium signaling and neuro-metabolic coupling in the brain. Neuroscience 323, 121–134. [PubMed: 25791228]

Rusakov DA, 2015. Disentangling calcium-driven astrocyte physiology. Nat Rev Neurosci 16, 226–233. [PubMed: 25757560]

Santuy A, Tomas-Roca L, Rodriguez JR, Gonzalez-Soriano J, Zhu F, Qiu Z, Grant SGN, DeFelipe J, Merchan-Perez A, 2020. Estimation of the number of synapses in the hippocampus and brain-wide by volume electron microscopy and genetic labeling. Sci Rep 10, 14014. [PubMed: 32814795]

Savtchouk I, Volterra A, 2018. Gliotransmission: Beyond Black-and-White. J Neurosci 38, 14–25. [PubMed: 29298905]

Schindelin J, Arganda-Carreras I, Frise E, Kaynig V, Longair M, Pietzsch T, Preibisch S, Rueden C, Saalfeld S, Schmid B, Tinevez JY, White DJ, Hartenstein V, Eliceiri K, Tomancak P, Cardona A, 2012. Fiji: an open-source platform for biological-image analysis. Nat Methods 9, 676–682. [PubMed: 22743772]

Semyanov A, Verkhratsky A, 2021. Astrocytic processes: from tripartite synapses to the active milieu. Trends Neurosci 44, 781–792. [PubMed: 34479758]

Sherwood MW, Arizono M, Hisatsune C, Bannai H, Ebisui E, Sherwood JL, Panatier A, Oliet SH, Mikoshiba K, 2017. Astrocytic IP3 Rs: Contribution to Ca(2+) signalling and hippocampal LTP. Glia 65, 502–513. [PubMed: 28063222]

Shigetomi E, Bushong EA, Haustein MD, Tong X, Jackson-Weaver O, Kracun S, Xu J, Sofroniew MV, Ellisman MH, Khakh BS, 2013. Imaging calcium microdomains within entire astrocyte territories

and endfeet with GCaMPs expressed using adeno-associated viruses. J Gen Physiol 141, 633–647. [PubMed: 23589582]

Stephan J, Eitelmann S, Zhou M, 2021. Approaches to Study Gap Junctional Coupling. Front Cell Neurosci 15, 640406. [PubMed: 33776652]

Swanson LW, Lichtman JW, 2016. From Cajal to Connectome and Beyond. Annu Rev Neurosci 39, 197–216. [PubMed: 27442070]

Tanaka M, Shih PY, Gomi H, Yoshida T, Nakai J, Ando R, Furuichi T, Mikoshiba K, Semyanov A, Itohara S, 2013. Astrocytic Ca2+ signals are required for the functional integrity of tripartite synapses. Molecular brain 6, 6. [PubMed: 23356992]

Tonnesen J, Inavalli V, Nagerl UV, 2018. Super-Resolution Imaging of the Extracellular Space in Living Brain Tissue. Cell 172, 1108–1121 e1115. [PubMed: 29474910]

Ullah G, Jung P, Cornell-Bell AH, 2006. Anti-phase calcium oscillations in astrocytes via inositol (1, 4, 5)-trisphosphate regeneration. Cell calcium 39, 197–208. [PubMed: 16330095]

Uylings HB, van Pelt J, 2002. Measures for quantifying dendritic arborizations. Network 13, 397–414. [PubMed: 12222821]

Ventura R, Harris KM, 1999. Three-dimensional relationships between hippocampal synapses and astrocytes. J Neurosci 19, 6897–6906. [PubMed: 10436047]

Witcher MR, Kirov SA, Harris KM, 2007. Plasticity of perisynaptic astroglia during synaptogenesis in the mature rat hippocampus. Glia 55, 13–23. [PubMed: 17001633]

Wolff JR, Stuke K, Missler M, Tytko H, Schwarz P, Rohlmann A, Chao TI, 1998. Autocellular coupling by gap junctions in cultured astrocytes: a new view on cellular autoregulation during process formation. Glia 24, 121–140. [PubMed: 9700495]

Wong-Riley MT, Trusk TC, Tripathi SC, Hoppe DA, 1989. Effect of retinal impulse blockage on cytochrome oxidase-rich zones in the macaque striate cortex: II. Quantitative electron-microscopic (EM) analysis of neuropil. Vis Neurosci 2, 499–514. [PubMed: 2562110]

Wyss MT, Weber B, Treyer V, Heer S, Pellerin L, Magistretti PJ, Buck A, 2009. Stimulation-induced increases of astrocytic oxidative metabolism in rats and humans investigated with 1–11C-acetate. J Cereb Blood Flow Metab 29, 44–56. [PubMed: 18714330]

Xu G, Wang W, Zhou M, 2014. Spatial organization of NG2 glial cells and astrocytes in rat hippocampal CA1 region. Hippocampus 24, 383–395. [PubMed: 24339242]

Yang Y, Vidensky S, Jin L, Jie C, Lorenzini I, Frankl M, Rothstein JD, 2011. Molecular comparison of GLT1+ and ALDH1L1+ astrocytes in vivo in astroglial reporter mice. Glia 59, 200–207. [PubMed: 21046559]

Zheng Z, Lauritzen JS, Perlman E, Robinson CG, Nichols M, Milkie D, Torrens O, Price J, Fisher CB, Sharifi N, Calle-Schuler SA, Kmecova L, Ali IJ, Karsh B, Trautman ET, Bogovic JA, Hanslovsky P, Jefferis G, Kazhdan M, Khairy K, Saalfeld S, Fetter RD, Bock DD, 2018. A Complete Electron Microscopy Volume of the Brain of Adult Drosophila melanogaster. Cell 174, 730–743 e722. [PubMed: 30033368]

Zhou M, Du Y, Aten S, Terman D, 2021. On the electrical passivity of astrocyte potassium conductance. J Neurophysiol 126, 1403–1419. [PubMed: 34525325]

Highlights:

- Astrocytes display spongiform morphology evolving from reflexive/leaflet processes
- Ultrastructural view of astrocyte-astrocyte contacts
- Ultrastructural view of spatial-location selectivity of astrocyte-synapse contacts
- Vesicle-like structures are scant throughout reconstructed astrocyte-connectome
- Astrocytes contain a dense mitochondrial network

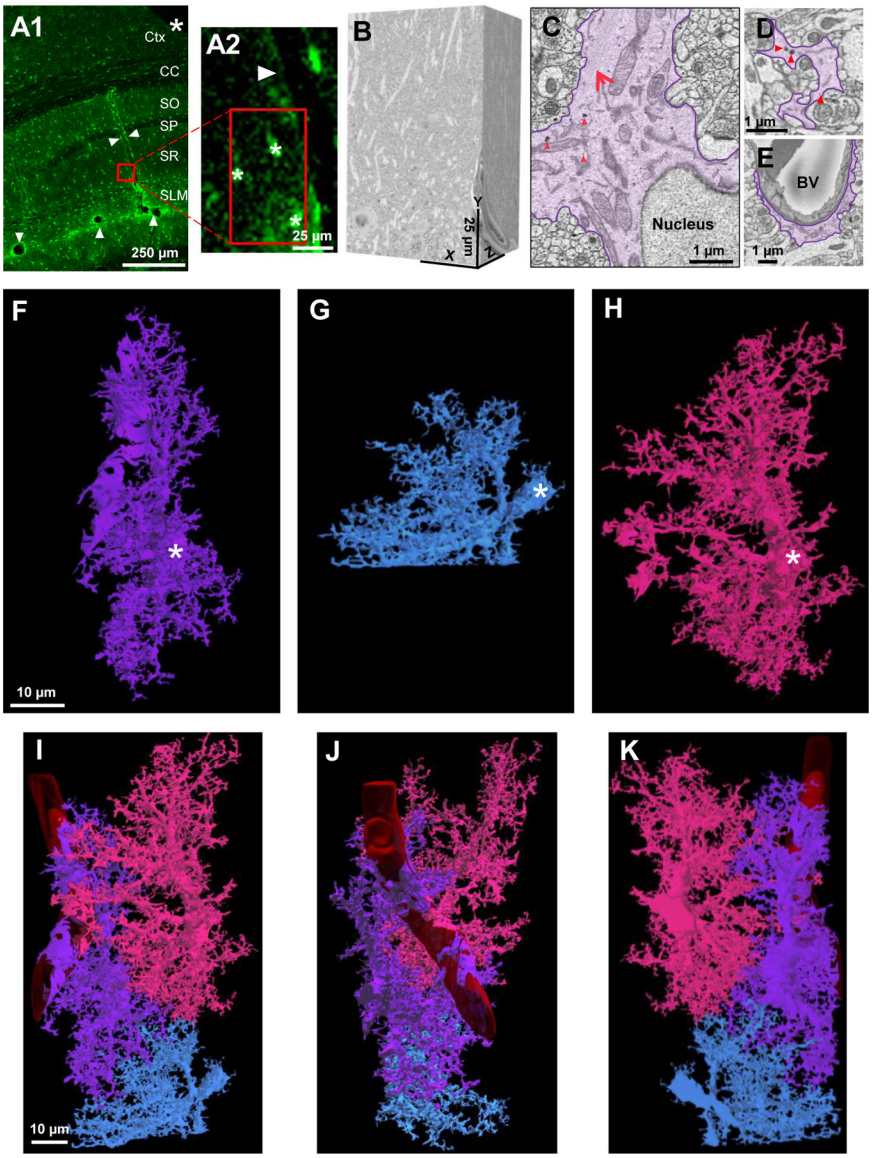

Figure 1. EM Identification and 3D reconstruction of neighboring astrocytes.

A1) Low magnification confocal microscope image of a fixed brain section displaying the location of eGFP^{+} astrocytes and delineation of blood vessels (white arrowheads). An angular cut (*) at the upper-right region of the tissue serves as a fiduciary mark. **A2)** A magnified area from **A1** shows the spatial location of 3 neighboring astrocytes next to a blood vessel. Asterisks (*) denote the 3 astrocytes observed in the SBF-SEM images. **B)** The resulting 500-stack SBF-SEM volume dataset from the selected ROI containing neighboring astrocytes from the *stratum radiatum* hippocampal subregion. **C)** An astrocyte was identified by first locating the nucleus-containing cell body. Bundles of filaments (large, red arrow) and several examples of glycogen granules (red arrowheads, also see Fig. S1) are noted near the astrocytic nucleus. **D)** Astrocyte processes (purple) that extend from the cell body possess an irregular and angular shape. **E)** Processes that contact blood vessels expand into specialized astrocyte endfeet processes. Abbreviations: Ctx-Cortex, CC-Corpus

callosum, SO-Stratum oriens, SP-Stratum pyramidale, SR-*stratum radiatum*, SLM-*stratum lacunosum-moleculare*, BV-blood vessel. **F-H)** 3-dimensional view of three reconstructed astrocytes: purple, blue, and pink. White asterisks found within each cell denote the somas, respectively. **I-K)** Combined reconstruction depicting the front, side, and back views of the three astrocytes. Each astrocyte is labeled in a different color to clearly demarcate individual astrocyte domains and cellular structures. Note that the blue astrocyte appears ‘smaller’ in size as only part of the cell was included in the EM stack.

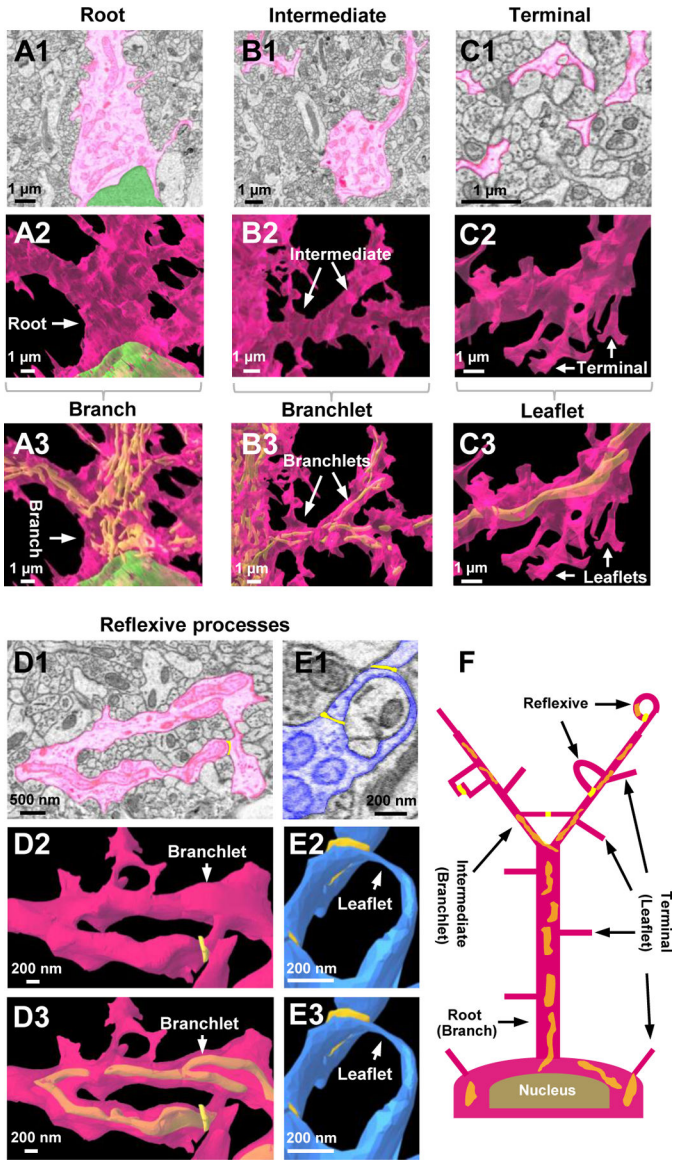

Figure 2. Ultrastructural view of astrocyte processes.

A1) 2D EM trace of an astrocyte root process. Root processes stem directly from the cell body of the astrocyte. The astrocyte nucleus is labeled in green. **A2-A3)** Reconstructed 3D view of an astrocyte root extending from the cell body. Similar to images in the top panels, the nucleus is shown in green. Note that the root processes are synonymous with previously defined astrocyte ‘branches’. Also note the mitochondria (in yellow) found within the astrocyte branch. The mitochondria (if present) can be observed in the bottom panel of all reconstructions depicted within this figure. **B1)** 2D EM trace of an astrocyte intermediate process extending from the root process. **B2-B3)** Reconstructed 3D view of astrocyte intermediate processes branching out from the root process. The intermediate processes are synonymous with previously defined astrocyte ‘branchlets’. Also note the mitochondria (in yellow) found within the branchlets. **C1)** 2D EM trace of terminal astrocyte processes. **C2-C3)** Reconstructed 3D view of astrocyte terminal processes extending from

an intermediate process. Note that terminal processes are smaller than root and intermediate processes; they reach a terminal (endpoint) and do not branch any further. These processes are synonymous with previously defined astrocyte ‘leaflets’. Note that no mitochondria is found within the leaflets. **D1)** 2D EM image and 3D reconstruction **(D2-D3)** of an astrocyte branchlet leading to a blood vessel. This process branches into two processes, which creates a reflexive contact near the endfoot process. Reflexive contacts are indicated in yellow in both the 2D images in the 3D images. Note that these reflexive contacts are depicted with a bright yellow color, relative to the lighter mitochondria, which are strictly found inside the astrocytes. **E1)** An EM image and 3D reconstruction **(E2-E3)** of a single leaflet process looping back to the branchlet. A distal leaflet process makes a reflexive contact near the top of the loop. Note that these reflexive processes are not completely fused (i.e., they do not form closed ‘loop’ structures). Also note that panels E2 and E3 are identical given that no mitochondria can be observed within the leaflets. **F)** Simplified schematic diagram depicting the astrocyte branching architecture and reflexive processes. Note that the diagram depicts both our astrocyte process terminology and the previously-defined branch, branchlet, leaflet terminology. Presumed contacts are noted in bright yellow, while internal mitochondria appears orange (given its location inside the pink astrocyte).

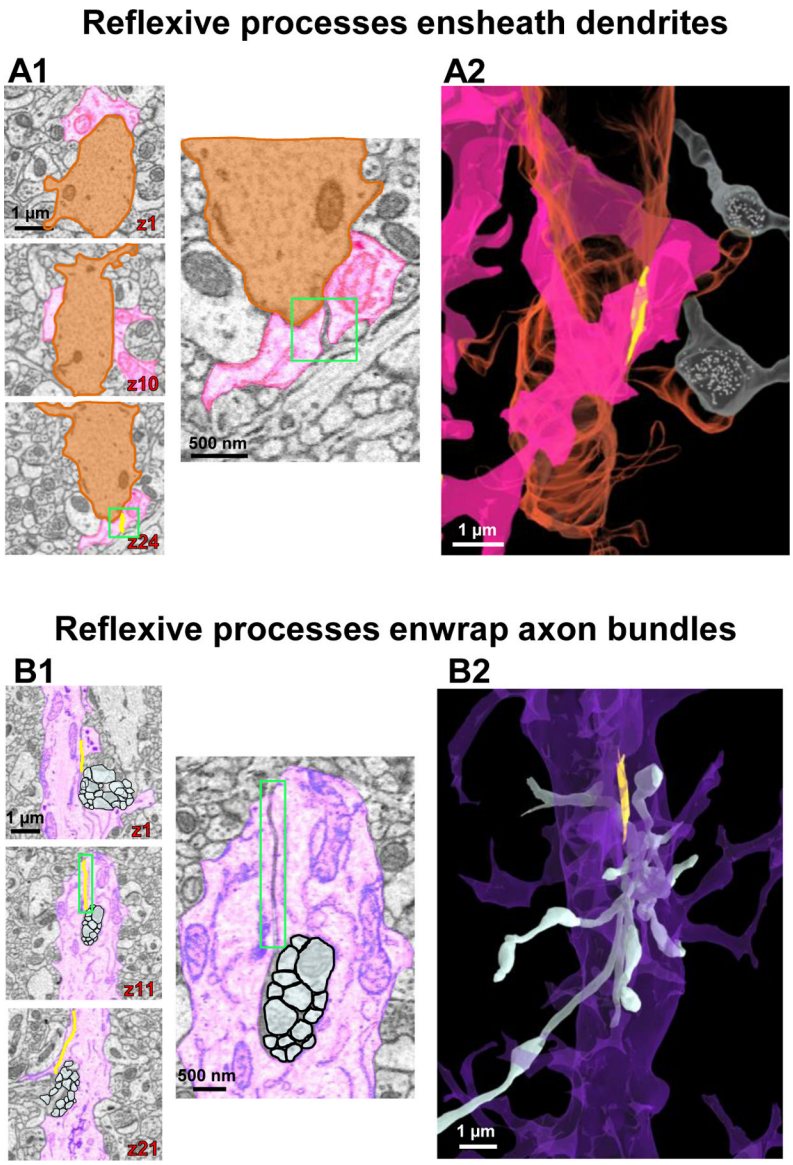

Figure 3. Astrocyte reflexive processes and their structural support to neurites.

A1) Serial 2D EM images of astrocyte branchlets (pink) encircling a dendritic shaft (orange). The bottom image in the left panel exhibits a reflexive contact (boxed in green). Higher magnification images in the right panel clearly show the contact depicted in z slice 24. **A2)** 3D reconstruction showing the astrocyte branchlets (pink) wrap around the dendrite (orange). Two axons (white) in synaptic contact with the associated dendritic spines are also represented. **B1)** 2D serial EM images of a branch point at the end of an astrocyte root process (purple) that splits into two branchlets, which enwrap a bundle of axons (white). Note the astrocyte reflexive contact in the middle panel (magnified on right side). **B2)** Side view of a 3D reconstruction of the axons (white) protruding through the enwrapment of the purple astrocyte process. All 3D reconstructions throughout the figure originated from the same astrocyte regions depicted in the corresponding 2D EM traces.

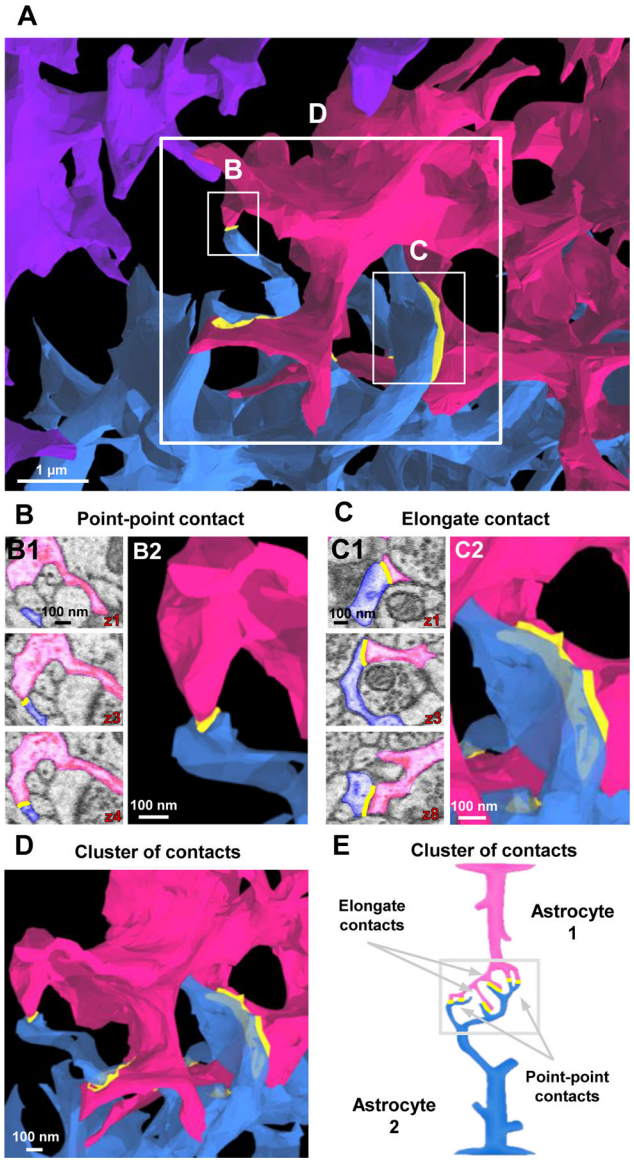

Figure 4. Contact patterns of astrocytes at their interfaces.

A) 3D reconstruction of astrocyte processes reveals the interface between the three astrocytes. For ease of viewing the ultrastructural inter-astrocyte contacts (between the pink and blue astrocytes), fewer intermediate and terminal processes were reconstructed in this image (relative to the images depicted in Fig. 1). Also note that contacts boxed in white are magnified in **B-D**. **B)** 2D serial EM images **(B1)** of point-point contacts between two astrocytes. These point-point contacts persist through a few serial sections to create a small contact at the tip of the terminal processes (see 3D EM image in **B2. C)** 2D serial EM images **(C1)** of an elongate contact. Elongate contacts typically contact/persist through many serial sections to create a large contact area (see 3D EM image in **C2**. **D)** A 3D reconstruction of a 'cluster of contacts'. This cluster of contacts contains a combination of both point-point and elongate contact types. **E)** Schematic diagram illustrating point-point contacts and elongate contacts that ultimately form a 'cluster of contacts'. Throughout the

figure, note that all 2D traces are from the same astrocyte region used to generate the 3D reconstructed images.

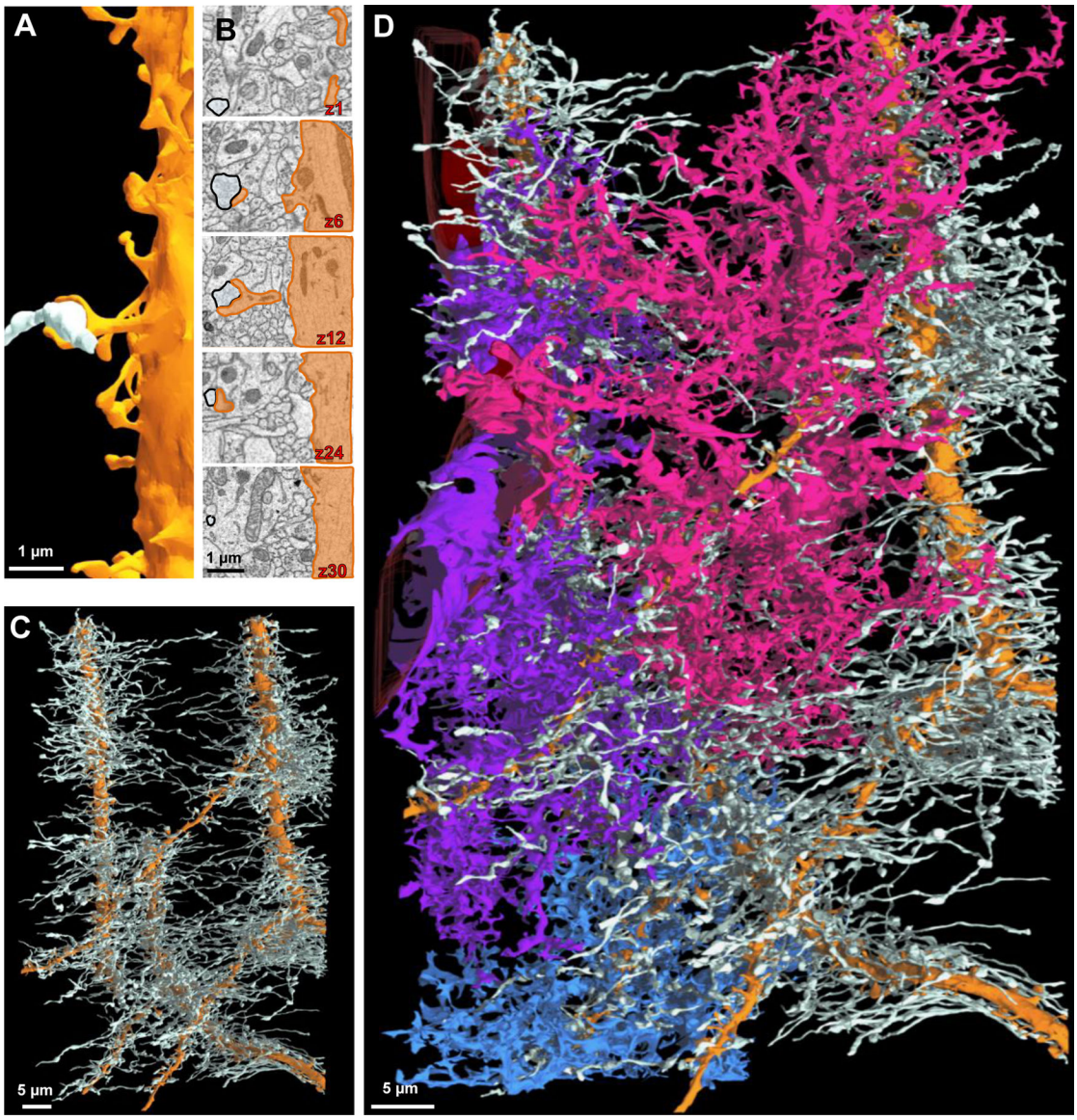

Figure 5. An ultrastructural view of astrocyte-neurite association.

A) Partial 3D reconstruction of one dendrite. An axon (white) is drawn for reference in order to depict the axon-dendritic spine interface (i.e., synapse). **B)** 2D serial traces of the axon (white) and dendritic spine (orange) that form a synapse (synapse is depicted in **A** and in z-section 12). **C)** 3D reconstruction of three dendrites (orange) and their associated axons (white) shown in a front view. **D)** Front view of the three neighboring astrocytes and their association(s) with the three reconstructed neurites.

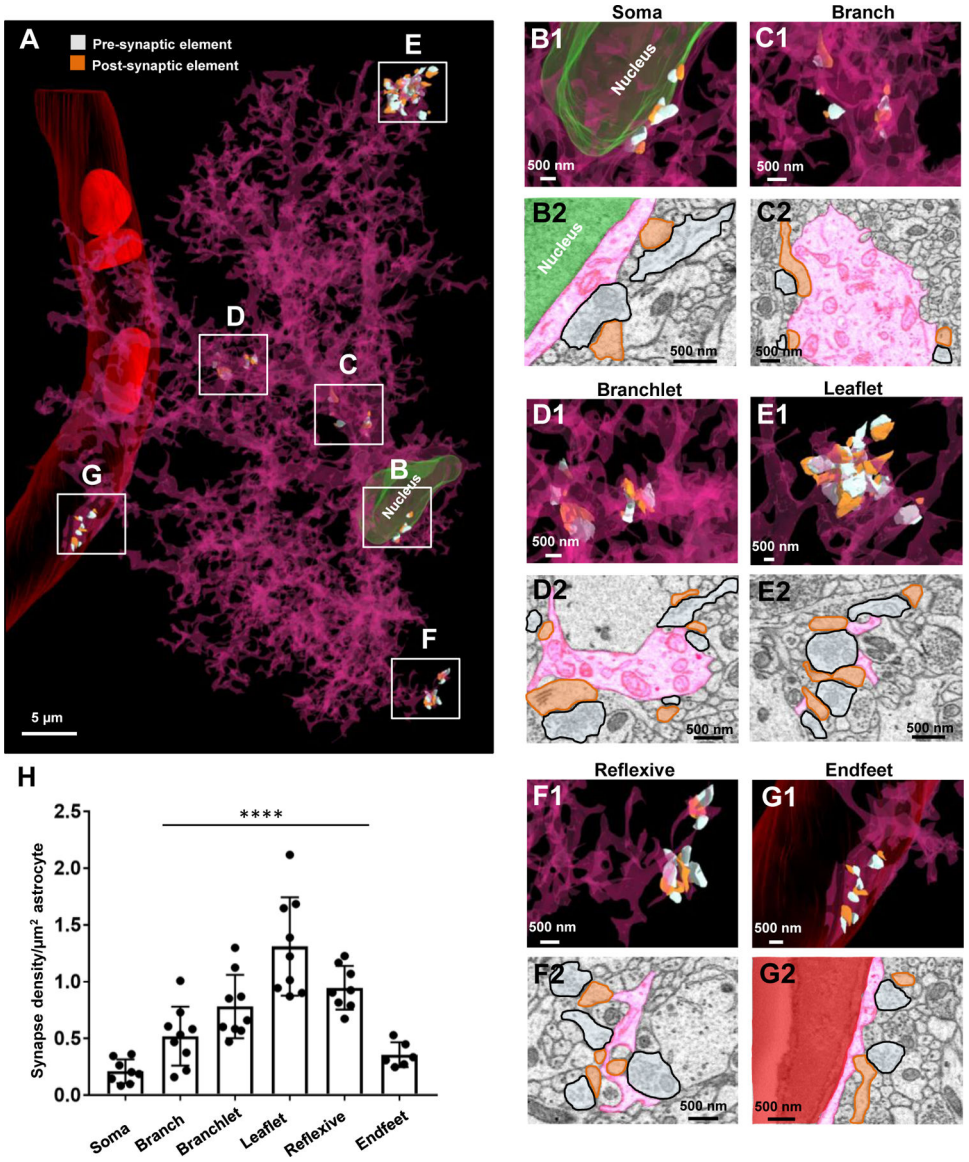

Figure 6. Synapses contact each compartment of an astrocyte, though an enrichment of synapses abut astrocytic leaflet and reflexive processes.

A) 3D reconstruction of an entire astrocyte (pink) and its contacts with synapses (orange: postsynapse and white: presynapse). Note that the white, boxed areas in **A** approximate the locations of magnified images in **B-G**. Further, the synapses depicted in the representative image **(A)** for each region were constructed from approximately the same volume of astrocyte. **B1)** Magnified 3D reconstruction of multiple synapses contacting the astrocyte soma. **B2)** 2D EM trace of synapses contacting the astrocyte soma. Note that the astrocyte nucleus is depicted in green in both the 2D and 3D images. **C1)** 3D reconstruction and 2D trace **(C2)** of synapses contacting an astrocyte branch. **D1)** 3D reconstruction and 2D trace **(D2)** of synapses contacting astrocyte branchlets. **E1)** 3D reconstruction and 2D trace **(E2)** of synapses contacting astrocyte leaflets. **F1)** 3D reconstruction and 2D trace **(F2)** of synapses contacting reflexive astrocyte processes. **G1)** 3D reconstruction and 2D trace **(G2)** of synapses contacting the astrocyte endfeet adjacent to the blood vessel (red). **H)**

Graphical representation of the synapse density per area of astrocyte. Data was obtained from three reconstructed astrocytes, with three ROIs chosen per astrocyte process region (soma, branch, branchlet, leaflet, reflexive, endfeet); represented as mean ± SEM. Note that one of three astrocytes (blue) did not contact a blood vessel, and thus only six ROIs are shown in the ‘endfoot’ panel of the graph. Also note that both branchlet and leaflet processes were included in the ‘reflexive’ analysis. ****: $p < 0.0001$; One-way ANOVA, followed by post-hoc tests.

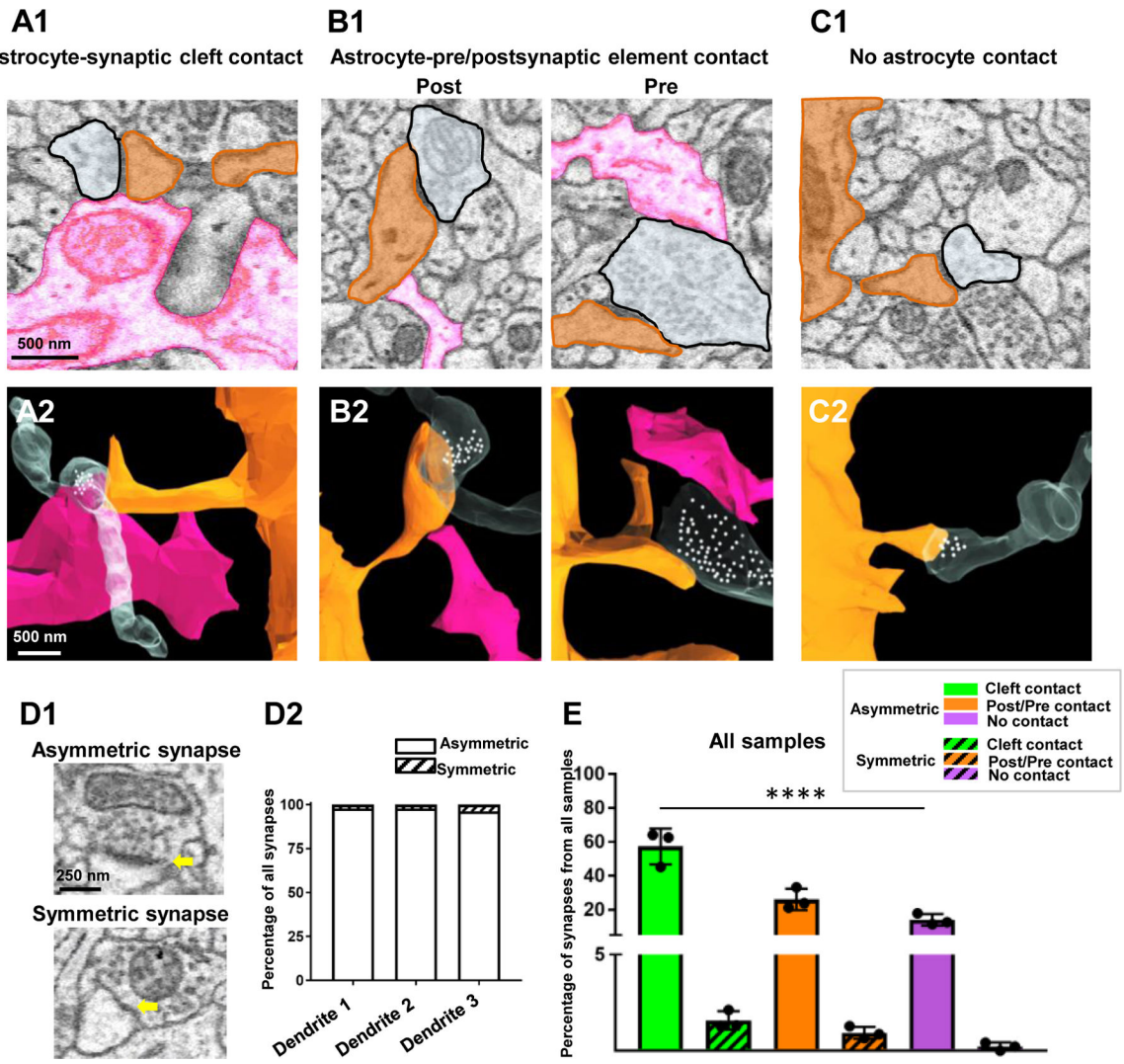

Figure 7. The majority of synapses are contacted by astrocytic processes.

A1) 2D EM trace of an astrocyte process (pink) contacting the synaptic cleft. **A2)** 3D reconstruction from **A1**. **B1)** 2D EM traces of astrocyte processes contacting either post-synaptic dendritic elements (left panel) or pre-synaptic elements (right panel). **B2)** 3D reconstruction from **B1**. **C1)** 2D EM trace of a synapse with no astrocyte contact. A 3D reconstruction is also depicted in **C2**. In all representative images, the astrocyte processes that contact the synapses are from one astrocyte (pink) and the synapses are from two fully reconstructed dendrites shown in Fig. 5. White spheres depict the approximate locations of synaptic vesicles observed from several serial 2D EM stacks. **D1)** 2D EM traces depict an example of an asymmetric synapse (prominent post synaptic density - top panel) and a symmetric synapse (modest post synaptic density - bottom panel). Yellow arrows denote the post-synaptic density. **D2)** Graphical representation of the percentage of asymmetric versus symmetric synapses (irrespective of astrocyte contact type) from all three traced dendrites. **E)** Graphical representation of the percentage of synapses (asymmetric or symmetric) that contact astrocyte processes at the synaptic cleft, on pre- or post-synaptic elements, or have no contact with astrocyte processes. Note that these data were pooled from the synapses

that contacted spines from all three reconstructed dendrites, and thus, each data point is representative of the percent coverage per dendrite. Data was analyzed by one-way ANOVA followed by post hoc tests; ****: $p < 0.0001$.

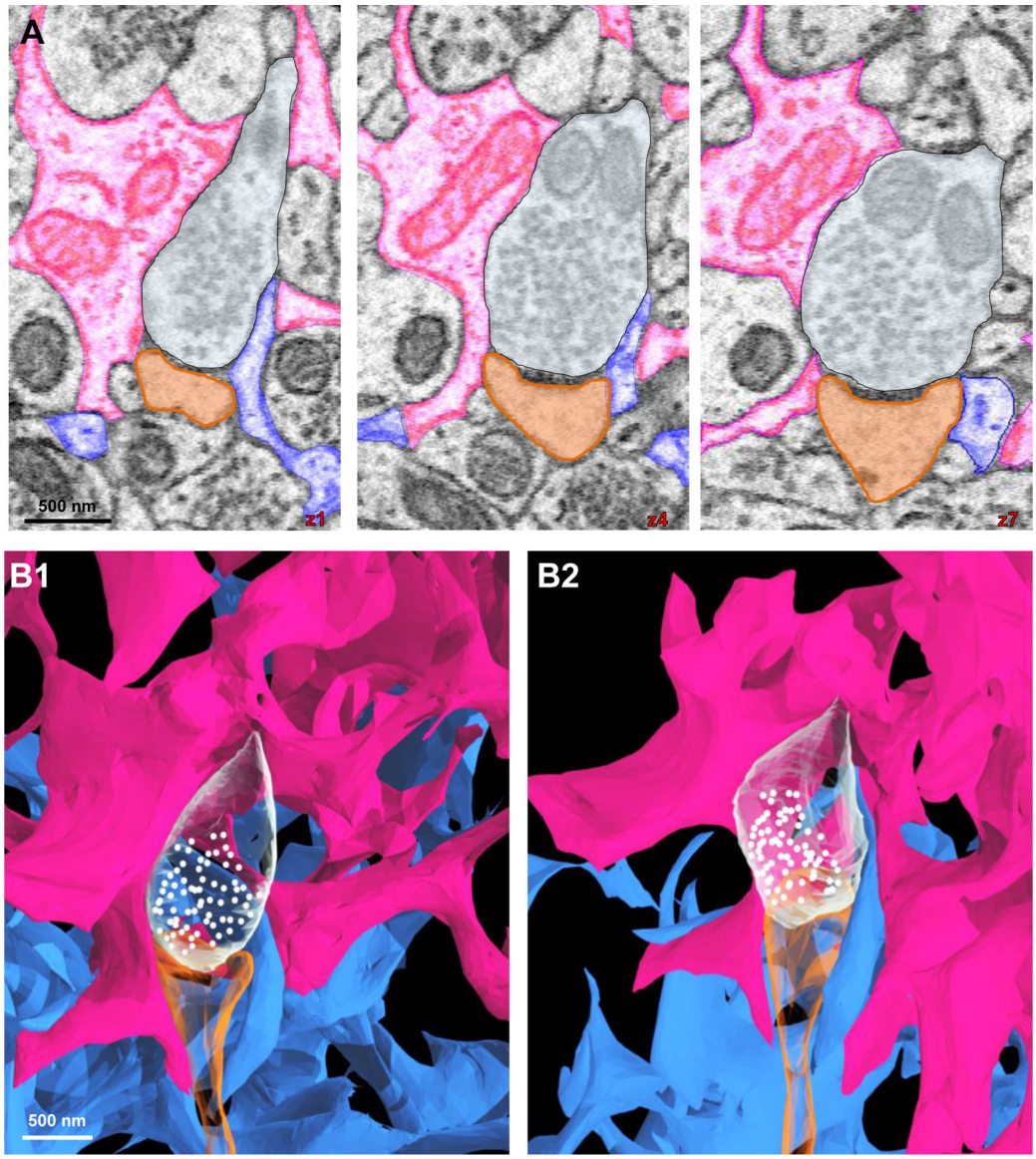

Figure 8. Synapses can be ensheathed by processes stemming from different astrocyte domains.

A) 2D serial EM traces of two astrocyte processes (pink and blue) contacting the same synapse (white: axon; orange: dendritic spine head). **B1-B2)** 3D reconstructions of the two astrocytes contacting the same synapse (from **A**). Note that as shown in the 2D traces, the pink process contacts the synapse on the left side and the blue process on the right side.

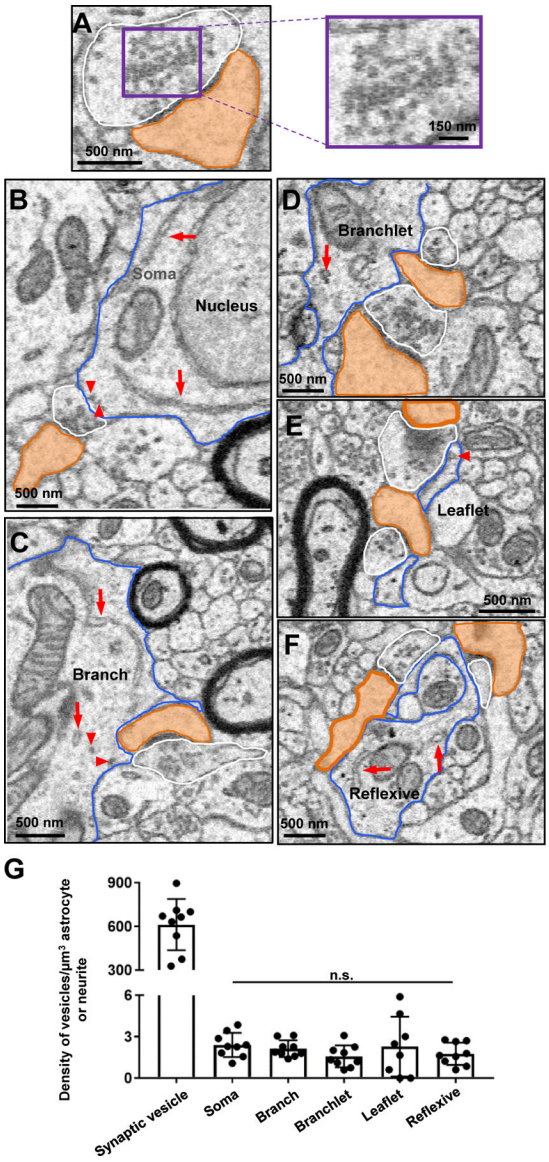

Figure 9. Paucity of vesicle-like structures in synapse-ensheathing astrocyte processes.

A) Representative 2D EM image of a synapse (white: pre-synaptic element; orange: dendritic spine head). Note the significant number of vesicles in the pre-synaptic element (magnified in the right panel). **B)** 2D EM traces of an astrocyte soma (blue outline), **(C)** astrocyte branch (blue outline), **(D)** astrocyte branchlet (blue outline), **(E)** astrocyte leaflet (blue outline), and **(F)** astrocyte reflexive process (blue outline). Synapses are also outlined (white: presynaptic element; orange: dendritic spine head). Note that very few (if any) presynaptic microvesicle-like structures were found in astrocyte processes that contacted synapses. Likely astrocyte vesicles are denoted by red arrowheads, and endoplasmic reticulum is denoted by long red arrows. **G)** Quantification of the approximate number of vesicle-like structures in each astrocyte (or neurite). Data is represented as mean ± SEM. No significant difference in the density of vesicle-like structures was found between process types. n.s.: not significant.

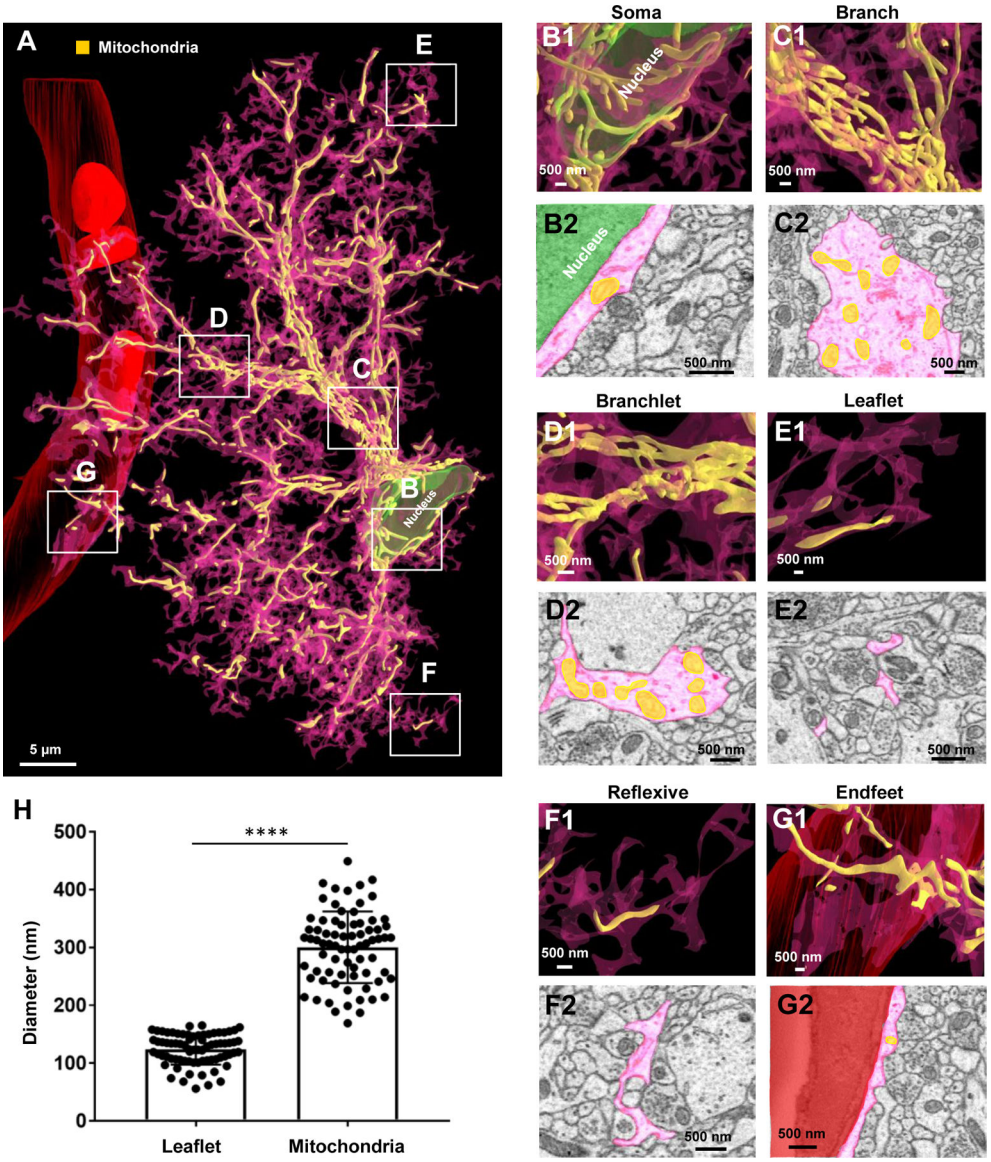

Figure 10. Extensive mitochondrial networks in astrocyte soma, branch, branchlet, reflexive, and endfeet processes.

A) 3D reconstruction of an entire astrocyte (pink) and its internal mitochondria (yellow). Note that the white, boxed areas in **A** approximate the locations of magnified images in **B-G**. **B1)** Magnified 3D reconstruction of mitochondria found within the astrocyte soma. **B2)** 2D EM trace of mitochondria within the astrocyte soma. Note that the astrocyte nucleus is depicted in green in both the 2D and 3D images. **C1)** 3D reconstruction and 2D trace **(C2)** of mitochondria within an astrocyte branch. **D1)** 3D reconstruction and 2D trace **(D2)** of mitochondria within astrocyte branchlets. **E1)** 3D reconstruction and 2D trace **(E2)** of mitochondria within astrocyte leaflets. **F1)** 3D reconstruction and 2D trace **(F2)** of mitochondria within reflexive astrocyte processes. **G1)** 3D reconstruction and 2D trace **(G2)** of mitochondria within an astrocyte endfoot adjacent to the blood vessel (red). **H)** Graphical representation depicting the average diameter of leaflet astrocyte processes, relative to the diameter of mitochondria. Each dot is indicative of the diameter of one leaflet process or one

mitochondria. The diameter of 25 leaflet processes and 25 mitochondria were measured for each of the three astrocytes. ****: $p < 0.0001$; student's t-test.

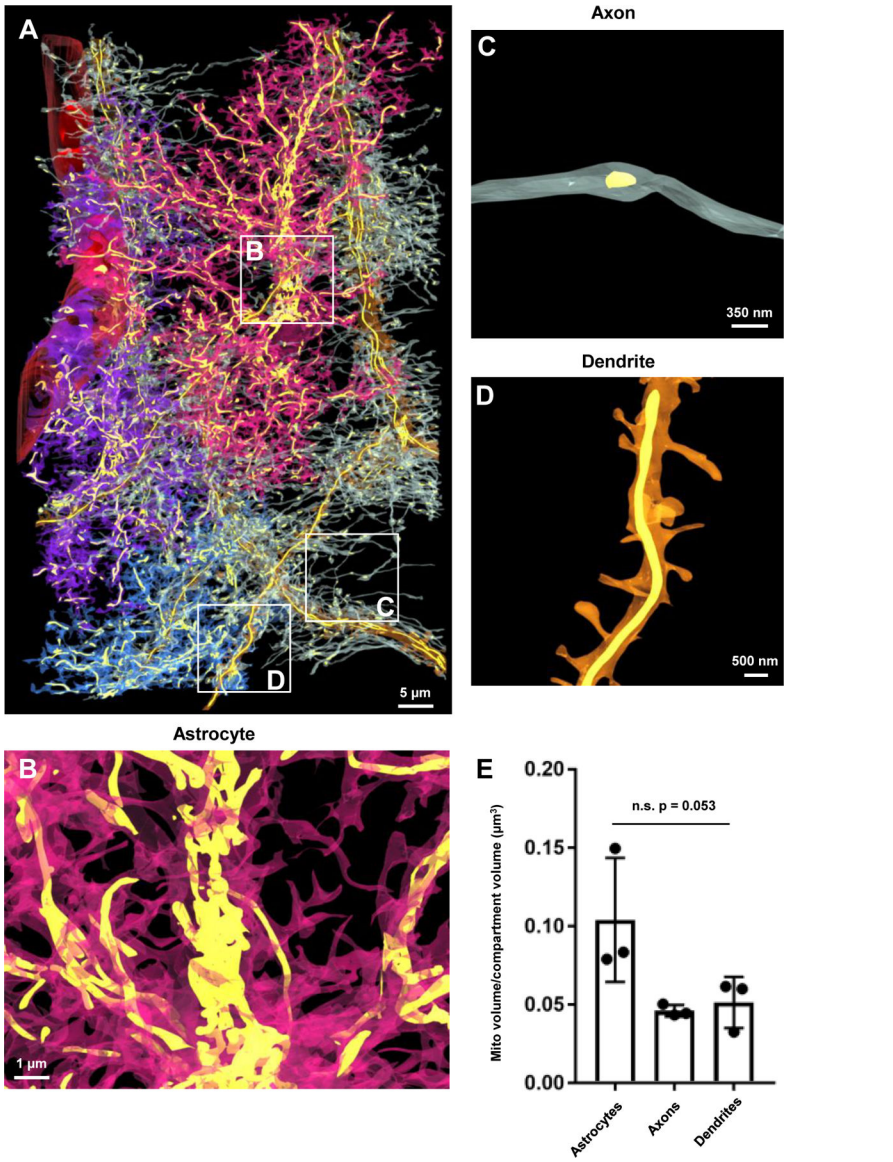

Figure 11. Astrocytes contain a similar quantity of mitochondria compared to neurites.

A) 3D reconstruction of the blood vessel, the three astrocytes, the three dendrites, and the associated axons and internal mitochondria (yellow) found within each structure. Note that the astrocytes and neurites were made partially transparent to visualize the mitochondria. Also note the white boxes in **A** reflect magnified images of mitochondria within an astrocyte **(B)**, an axon **(C)** and a dendrite **(D)**. **E)** Graphical representation of the mitochondria to cell volume ratio for astrocytes and neurites. Note that each point on the graph is representative of the mitochondria to volume ratio of the entire structure (i.e., one of three reconstructed astrocytes, dendrites, or all of the axons from one dendrite). n.s.: not significant; One-way ANOVA.